



## Air–Sea Turbulent Heat Fluxes in Climate Models and Observational Analyses: What Drives Their Variability?

R. JUSTIN SMALL AND FRANK O. BRYAN

*National Center for Atmospheric Research, Boulder, Colorado*

STUART P. BISHOP

*North Carolina State University, Raleigh, North Carolina*

ROBERT A. TOMAS

*National Center for Atmospheric Research, Boulder, Colorado*

(Manuscript received 31 August 2018, in final form 4 January 2019)

### ABSTRACT


A traditional view is that the ocean outside of the tropics responds passively to atmosphere forcing, which implies that air–sea heat fluxes are mainly driven by atmosphere variability. This paper tests this viewpoint using state-of-the-art air–sea turbulent heat flux observational analyses and a climate model run at different resolutions. It is found that in midlatitude ocean frontal zones the variability of air–sea heat fluxes is not predominantly driven by the atmosphere variations but instead is forced by sea surface temperature (SST) variations arising from intrinsic oceanic variability. Meanwhile in most of the tropics and subtropics wind is the dominant driver of heat flux variability, and atmosphere humidity is mainly important in higher latitudes. The predominance of ocean forcing of heat fluxes found in frontal regions occurs on scales of around 700 km or less. Spatially smoothing the data to larger scales results in the traditional atmosphere-driving case, while filtering to retain only small scales of 5° or less leads to ocean forcing of heat fluxes over most of the globe. All observational analyses examined (1° OAFflux; 0.25° J-OFURO3; 0.25° SeaFlux) show this general behavior. A standard resolution (1°) climate model fails to reproduce the midlatitude, small-scale ocean forcing of heat flux: refining the ocean grid to resolve eddies (0.1°) gives a more realistic representation of ocean forcing but the variability of both SST and of heat flux is too high compared to observational analyses.

### 1. Introduction

Recent studies have shown that air–sea flux variability associated with oceanic small-scale features such as mesoscale eddies has a different character from that associated with broader basin scales. Much attention has been paid to the air–sea momentum flux variability (Xie et al. 1998; Chelton et al. 2001; Small et al. 2008; Schneider and Qiu 2015) but less to the air–sea turbulent heat flux variability.

Air passing over the relatively strong gradients of sea surface temperature (SST) associated with eddies and fronts is forced out of equilibrium with the underlying sea surface. Large differences between SST and air temperature arise, and also between the air humidity and the saturated humidity at the ocean surface temperature, especially under strong background wind speeds (Xie 2004; Hausmann et al. 2017). The resulting changes to surface stability and roughness, and also changes to wind speed (Small et al. 2008), give rise to the anomalies in surface heat flux. More heat flux out of the ocean is seen over warm SST, and less upward heat flux over the colder SST. Hence there is a positive correlation between surface heat flux and SST, where the sign convention used throughout this paper is that positive heat flux denotes heat loss from the ocean. At lower

---

 Supplemental information related to this paper is available at the Journals Online website: <https://doi.org/10.1175/JCLI-D-18-0576.s1>.

---

*Corresponding author:* R. Justin Small, [jsmall@ucar.edu](mailto:jsmall@ucar.edu)

DOI: 10.1175/JCLI-D-18-0576.1

© 2019 American Meteorological Society. For information regarding reuse of this content and general copyright information, consult the [AMS Copyright Policy](#) ([www.ametsoc.org/PUBSReuseLicenses](http://www.ametsoc.org/PUBSReuseLicenses)).

background wind speeds the atmosphere temperature and humidity will adjust more to the rapidly changing SST, and the heat flux anomalies will be weaker (Hausmann et al. 2017).

The behavior described above contrasts with that seen at larger scales, where heat loss from the ocean would be associated with a cooling of the ocean (Xie 2004, and references therein). In that case the overlying air is more in equilibrium with the slow sea surface temperature changes: there is very small simultaneous correlation between heat flux and SST, but the SST responds in a lagged fashion to the heat flux.

These relationships have been encapsulated in idealized stochastic models of air–sea interaction by, for example, Frankignoul and Hasselmann (1977), Barsugli and Battisti (1998), von Storch (2000), and Wu et al. (2006). As reviewed in Bishop et al. (2017), when these models include a substantial amount of atmosphere noise (i.e., the weather systems), the SST tendency responds to the approximated air–sea heat flux term, giving a negative simultaneous correlation between heat flux and SST tendency, and also near-zero simultaneous correlation between SST and heat flux. In contrast, when the oceanic noise term is strong, there is near-zero simultaneous correlation between heat flux and SST tendency, but heat flux and SST has a positive simultaneous correlation [see summary Fig. 1 in Bishop et al. (2017)].

In the latter case, the SST is not forced locally by the air–sea heat flux, and thus we refer to the SST variability as intrinsic variability in this paper. (Note that on monthly time scales, as will be shown later, most of the air–sea interactions are quite local; in other words, the SST anomaly does not move far on monthly time scales.) This definition follows the finding by Sérazin et al. (2015) that in high-resolution models most of the small-scale SSH variability is intrinsic, and intrinsic motions also contribute in a nonnegligible fashion to large-scale variability of SSH. This notion will be expanded upon in a follow-on paper that aims to separate out the contributions of heat content variability due to atmosphere-forcing by air–sea heat fluxes, versus atmosphere forcing by Ekman heat fluxes, versus oceanic motions.

The relationship of surface heat flux to SST has applications to atmosphere variability (Kuo et al. 1991; Ma et al. 2017) and to ocean variability (Ma et al. 2016). It is therefore useful to know whether climate models reproduce the surface heat flux response. Kirtman et al. (2012) briefly discussed the different air–sea heat flux behavior of coupled models with low versus high ocean resolution. They found that the case with a high-resolution ocean gave results consistent with the stochastic model described above with strong “oceanic

noise,” and the low-resolution case was consistent with a more pure atmospheric noise driving. Smirnov et al. (2014) used a linear inverse model, applied to observational analyses and the Kirtman et al. (2012) model runs, to show that most of the SST variability in the Kuroshio and Oyashio Extension systems was intrinsic to the ocean, whereas in the northeast Pacific Ocean it was driven by the atmosphere.

Roberts et al. (2016) found that both an eddy-resolving and an eddy-permitting ocean model gave similar ocean-driven results when employed in a fully coupled system. Putrasahan et al. (2017) looked at the air–sea interaction processes in the Gulf of Mexico in detail, showing that the high-resolution climate model of Kirtman et al. (2012) agreed with the observed ocean driving of heat fluxes at monthly time scales, and further found that oceanic advection gave rise to the SST anomalies that drove the surface heat flux.

In this paper we will update and expand on the observational and modeling results discussed above, and make a detailed assessment of the ability of climate models to reproduce the observed behavior. In particular we analyze the causes of air–sea heat flux variability in state-of-the-art high-resolution air–sea heat flux products, and in the Community Earth System Model version 1 (CESM1; Hurrell et al. 2013).

For submonthly time scales, synoptic atmosphere variability dominates heat flux variability in many storm track locations (see section 5b). Meanwhile for decadal and longer-term variability, the observational record is short, although some interesting findings have been made for subpolar gyre variability on these time scales by, for example, Gulev et al. (2013), Clement et al. (2015), Zhang et al. (2016), Delworth et al. (2017), Cane et al. (2017), and O’Reilly and Zanna (2018). For these reasons, we focus on monthly to interannual variability, at which frequency ocean eddy variability is strong, so that the inclusion of small scales in the ocean is more likely to have a notable impact, and there is sufficient data for analysis.

In particular we address the following questions:

- 1) How much of turbulent heat flux variance is explained by SST variability versus atmosphere state variability (wind, air temperature, and air humidity)?
- 2) How realistic are the models, for different resolutions, in terms of SST and heat flux variances, and their correlation?
- 3) Do the scales of variability in the model match observations?

The paper is organized as follows: Section 2 describes the model and observed product data, and the methods of analysis, including latent heat flux (LHF)

decomposition and feedback parameter. LHF is focused on because of its dominance of the net heat flux term response to SST (see [section 2](#) below). [Section 3](#) describes the variability and covariability of SST and LHF in models and data, and then [section 4](#) presents two methods of fully decomposing the LHF variability into parts due to SST, wind, and humidity. [Section 5](#) covers the scale dependence of the SST–LHF relationship as a function of space and time. [Section 6](#) discusses further questions about SST variability, the transition scale, and the response of the atmosphere and ocean to the fluxes. This is followed by conclusions in [section 7](#).

## 2. Methods

### *a. Models*

CESM1 as applied here is composed of the Community Atmosphere Model 5.2 using a spectral element dynamical core ([Park et al. 2014](#)), Parallel Ocean Program version 2 (POP2; [Smith et al. 2010](#)), Community Ice Code version 4 ([Hunke and Lipscomb 2008](#)), Community Land Model version 4 ([Lawrence et al. 2011](#)), and CESM Coupler 7 with the [Large and Yeager \(2009\)](#) air–sea flux routine. The highest-resolution simulation used here, with  $0.25^\circ$  resolution in the atmosphere and nominal  $0.1^\circ$  in the ocean, is described in full in [Small et al. \(2014\)](#). It was run for 100 years under “present-day” (year 2000) greenhouse gas conditions and is referred to here as CESM-High Ocean Resolution (CESM-HR). This is compared to a simulation with the same  $0.25^\circ$  atmosphere resolution but a nominal  $1^\circ$  ocean resolution, where ocean eddies are parameterized ([Gent and McWilliams 1990](#)). This 90-yr run under fixed year 2000 conditions is referred to as CESM-Low Ocean Resolution (CESM-LR). [It is different from the CESM with standard resolution described in [Small et al. \(2014\)](#), which had an atmosphere resolution of  $1^\circ$ .] For both simulations, 35 years of data from the end of the run have been analyzed.

### *b. Observational products of SST and latent heat flux*

In this paper the observational analysis of SST used as a benchmark is [Reynolds et al. \(2007\)](#), a daily dataset of  $0.25^\circ$  SST obtained from satellite and in situ data. The in situ and satellite data are combined using optimal interpolation with error correlation scales ranging from 50 km in western boundary currents and their extensions (referred to together in this paper as WBCs) to 200 km. A dataset with satellite data from AVHRR is available (starting in 1981), as is a dataset with both AVHRR and AMSR (2002–11 only). We use the AVHRR-only dataset for its greater length and avoiding any jump

issue with including AMSR. The AVHRR dataset will have reduced sampling on a daily basis due to the persistent cloud cover over WBCs ([Reynolds et al. 2013](#)); however, for our purposes a comparison of monthly SST variability from the two products for their common length of record revealed negligible differences. The [Reynolds et al. \(2007\)](#) dataset will be referred to by OISST in the remainder of this paper. Note that for analysis of the correlation (or related statistics) between SST and LHF for observational analyses listed next, the SST provided with the analysis is used.

For analyses of air–sea heat fluxes, a number of products exist in the community, based on in situ data, satellite data, reanalysis data, or some combination of these. As shown in, for example, [Jin and Yu \(2013\)](#) and [Zhang et al. \(2018\)](#), the products give a wide range of turbulent heat flux values, both for climatology and for variability. It is not the aim of this paper to choose the “best” product due to the large spread in analysis products and limited validation datasets (buoys etc.). Instead we choose three representative analyses of air–sea heat fluxes: one blended dataset, which should not be biased too much to a particular data source, and two high-resolution and mainly satellite-based datasets, as our main interest is in small scales.

The Japanese Ocean Flux Datasets with Use of Remote Sensing Observations version 3 (J-OFURO3) is the evolution of the original J-OFURO dataset ([Kubota et al. 2002](#); [Tomita et al. 2010](#)). The new version is available for 1996–2013 with daily and monthly-mean temporal resolution at  $0.25^\circ$  spatial resolution. The focus of this study is on the monthly mean output. The dataset is derived solely from satellite data except for 2-m air temperature taken from the NCEP–DOE reanalysis ([Kanamitsu et al. 2002](#)). Daily averaged SST is an ensemble median of multiple satellite data sources and of [Reynolds et al. 2007](#) OISST. The fluxes are computed using the COARE 3.0 bulk flux algorithm ([Fairall et al. 2003](#)). We use the latter years 2002–13 when more satellite data was available. Full details of the dataset are given in [Tomita et al. \(2019\)](#).

The Objectively Analyzed Air–Sea Fluxes (OAFlux) product ([Yu and Weller 2007](#)) uses variational objective analysis to combine satellite retrievals of wind and humidity and SST with reanalysis data of the same variables and also air temperature. The COARE 3.0 bulk flux algorithm ([Fairall et al. 2003](#)) was used to compute bulk fluxes. The product is available at  $1^\circ$  for global ice-free oceans and extends from 1958 to near present, with the period prior to the 1980s being governed by reanalysis-only data [NCEP–NCAR ([Kalnay et al. 1996](#)) and ERA-40 ([Uppala et al. 2005](#))]. The analysis here uses monthly-averaged LHF data from 1985–2014. Note

that a high-resolution ( $0.25^\circ$ ) version of OAFlux is under development [L. Yu 2018, personal communication; Jin and Yu (2013) use a preliminary version] but is not used here.

SeaFlux is a global dataset of surface turbulent heat fluxes and associated variables compiled 3 hourly and at  $0.25^\circ$  from 1998. In contrast to the above products, all variables and fluxes are derived from satellite data. A neural network approach is used to derive the near-surface atmospheric temperature and humidity (Roberts et al. 2010). Daily averaged SST is obtained from Reynolds et al. (2007) OISST and SSMI brightness temperatures. Diurnally varying SST is parameterized and used for the fluxes (Clayson and Bogdanoff 2013). Further details can be found in Roberts et al. (2010) and Clayson and Bogdanoff (2013). As with the above datasets, SeaFlux uses the COARE 3.0 for bulk fluxes (Fairall et al. 2003).

### c. Analysis methods

This paper focusses on the LHF component of the net surface heat flux. The reason for this is that many previous studies have identified that the LHF response to SST dominates the net flux response, with much smaller contributions from sensible heat fluxes and the radiative fluxes (e.g., Frankignoul and Kestenare 2002; Park et al. 2005). Part of this is to be expected from the Bowen ratio [ratio of sensible heat flux to LHF; see, e.g., Andreas et al. (2013) for a detailed study of the Bowen ratio], which is typically much less than 1.

LHF is given in bulk flux form as

$$Q_E = \rho_a L C_E U_a (q_s - q_a), \quad (1)$$

where  $U_a$  is the low-level (typically 10 m) wind speed and  $q$  is specific humidity, with subscripts  $s$  and  $a$  denoting sea and air;  $q_s$  is the saturated specific humidity at the surface temperature, and  $q_a$  is measured near the surface, often at 2 m. Also,  $L$  is the latent heat of vaporization,  $C_E$  is the turbulent exchange coefficient for moisture, derived from Monin–Obukhov similarity theory (e.g., Liu et al. 1979; Large and Yeager 2004; Fairall et al. 1996), and  $\rho_a$  is the low-level air density.

For the main data analysis, monthly mean data are either gathered directly from the data providers or, if not available, derived from the original daily or 3-hourly

data. The monthly climatology is then computed for the appropriate length of record for each analysis, with anomalies defined as the deviation of the monthly data from the monthly climatology. A linear trend is removed.

The focus of this paper is on small-scale local interaction, and so the influence of ENSO on equatorial and remote heat fluxes and SST is reduced by removal of the linear regression on Niño-3.4 SST, as shown in Figs. S1 and S2 in the online supplemental material. This was done for all variables. A more sophisticated method based on removing the first three principal components of tropical Pacific SST was also tried [based on the appendix of Frankignoul et al. (2011)], but this made negligible difference to the results in midlatitudes.

For the investigation of interannual variability, annual-mean data are used, and the anomaly defined as the annual average minus the long-term mean. ENSO effects were reduced in this case by removing the Niño-3.4 regression using two methods: first using annual-mean data, which might mix phases of ENSO, then by using monthly mean data for the removal of regression on Niño-3.4, and then computing annual averages. Both methods gave similar results, and the former is shown here.

In section 3, the focus is on the SST–LHF and  $\partial\text{SST}/\partial t$ –LHF relationships. Instantaneous linear correlations (Pearson’s method of dividing covariance by the standard deviations) are performed at each grid point. In all examples in this paper of correlations between two variables, it is understood that the above-defined anomalies are used. SST tendency is defined using centered difference of monthly anomalies. The utilized grid spacing is  $0.25^\circ$  for all observational datasets and model data except the  $1^\circ$  OAFlux. Global maps are then produced of these gridscale relationships. Section 4 similarly describes gridscale relationships while section 5 specifically looks at the effect of analysis on different spatial scales and temporal lags.

### d. Latent heat flux decomposition methodology

Following Cayan (1992), Alexander and Scott (1997), and Tanimoto et al. (2003), the bulk formula for LHF is written in terms of time-mean quantities and anomalies, so that anomalies of LHF are given as

$$Q'_E = Q_E - \bar{Q}_E = \rho_a L C_E \left\{ \underbrace{\bar{U}_a q'_s}_{(i)} - \underbrace{\bar{U}_a q'_a}_{(ii)} + \underbrace{U'_a (\bar{q}_s - \bar{q}_a)}_{(iii)} + \underbrace{[U'_a (q'_s - q'_a) - \bar{U}'_a (q'_s - q'_a)]}_{(iv)} \right\}, \quad (2)$$

where overbars denote time mean and primes are deviations from the mean. (In practice we use climatological monthly means for overbar terms and deviations from climatological means for deviation terms.) Two types of decompositions of the LHF variability are performed in this paper. All regression coefficients are obtained by standard least squared fits.

### 1) METHOD 1: PARTIAL REGRESSION METHOD

In the first method the LHF is regressed onto the variables  $U_a$ ,  $q_a$ , and SST. Following standard practice we use SST instead of  $q_s$  as  $q_s'$  is an approximately linear function of SST' over a small range of SST'. This was confirmed by a comparison of correlation of SST and LHF, and of  $q_s$  with LHF: the two correlation fields were almost identical (not shown). Initially a standard univariate linear regression was performed sequentially for each variable, but this gave poor results as  $U_a$ ,  $q_a$ , and SST are not independent, as shown in the supplemental text and Figs. S3 and S4. This motivated us to try the partial regression technique (Cohen and Cohen 1983; Saji and Yamagata 2003). Here, for example, if  $U_a' = \gamma \text{SST}' + U'$ , where  $\gamma$  is the linear regression coefficient of  $U_a$  on SST, then  $U'$  is a time-varying residual, which is the  $U_a$  variation not linearly dependent on SST. The variable  $U'$  is then correlated or regressed on the LHF.

The full technique is given by

$$Q'_E = ASST' + BU' + CQA', \quad (3a)$$

where partial regression is used:

$$U' = U'_a - \gamma \text{SST}', \quad (3b)$$

$$QA' = q'_a - \epsilon U' - \pi \text{SST}'. \quad (3c)$$

Here  $U$  is the wind anomaly with dependence on SST removed, and QA is the humidity anomaly with dependence on wind and on SST removed. Also,  $A$  is the regression coefficient of LHF on SST,  $\gamma$  is the regression of  $U_a$  on SST,  $\epsilon$  is the regression of  $q_a$  on wind,  $\pi$  is the regression of  $q_a$  on SST,  $B$  is the regression of LHF on residual wind  $U$ , and  $C$  is the regression of LHF on residual humidity QA.

### 2) METHOD 2: FULL DECOMPOSITION

Method 1 ignores some details, such as the role of the exchange coefficient in (2), and does not explicitly show the covariances (although the partial regression technique attempts to account for some of the covariance). The second method is to explicitly decompose the LHF using (2), following Cayan (1992) and Alexander and Scott (1997), who analyzed earlier datasets. This has been done for the high-resolution coupled simulation

CESM-HR, where daily data of LHF, SST, low-level wind, and humidity were saved in a 10-yr segment of the run. From this the exchange coefficient  $C_E$  is estimated daily from the standard bulk formula (1) where all variables except  $C_E$  are known (here we need to derive  $q_s$  from SST). This method generally worked well in providing robust estimates of  $C_E$  except in some storm track regions where subdaily variability was large, which led to noise in the derived data. The daily estimates are then used to form monthly averages of  $C_E$  and also an approximate monthly climatology from the 10-yr segment. For the monthly climatology the noise referred to above was treated, by applying running box averages over a full-width equivalent to 1° of latitude, where the outliers (values of  $C_E < 5 \times 10^{-4}$  or  $C_E > 2 \times 10^{-3}$ ) were not included (typical estimates of  $C_E$  are  $1 \times 10^{-3}$  to  $1.5 \times 10^{-3}$ ; Liu et al. 1979; Fairall et al. 1996; Large and Yeager 2004). This led to smooth fields of climatological  $C_E$  that are used to compute (2) in section 4b.

Each term in (2) is then known for the 10-yr segment, while for analysis of a longer record of the model run the decomposition is performed under the approximation that  $C_E$  in (2) is equal to the climatological monthly value. In the appendix the full LHF anomaly is regressed on each term on the RHS of (2), including the contribution from  $C_E$  variability, for the 10-yr segment. This approach is similar in concept to that of Doney et al. (2007), who regressed heat budget terms onto total tendency in the ocean to assess their relative importance. Further, in section 4b, the smooth climatological  $C_E$  is used to facilitate the decomposition for a longer (35 year) segment of the CESM-HR model run, for comparison with method 1.

### 3. Variability and covariability of SST and latent heat flux

#### a. Monthly data (subseasonal variability and longer time scales)

Before analyzing the covariability of SST and LHF, we set the scene by presenting the variability of SST and LHF separately. Here we mainly use J-OFURO3 for analysis of LHF, together with OISST for SST variability, but results from other LHF datasets are discussed below.

The standard deviation of monthly SST variability in OISST reaches maxima of around 1°–2°C in the WBCs and Agulhas Return Current (Fig. 1a). Note that much of the tropical SST variability was removed by regressing out the Niño-3.4 dependence (see Figs. S1 and S2). Two main conclusions can be drawn by comparing the model results (Fig. 1b,c) with the observational estimates (Fig. 1a). First, the pattern of SST variability in the high-resolution simulation is much closer to observations than in the low-resolution case. Second, however, the high-resolution model has too much SST variability in the WBCs, and

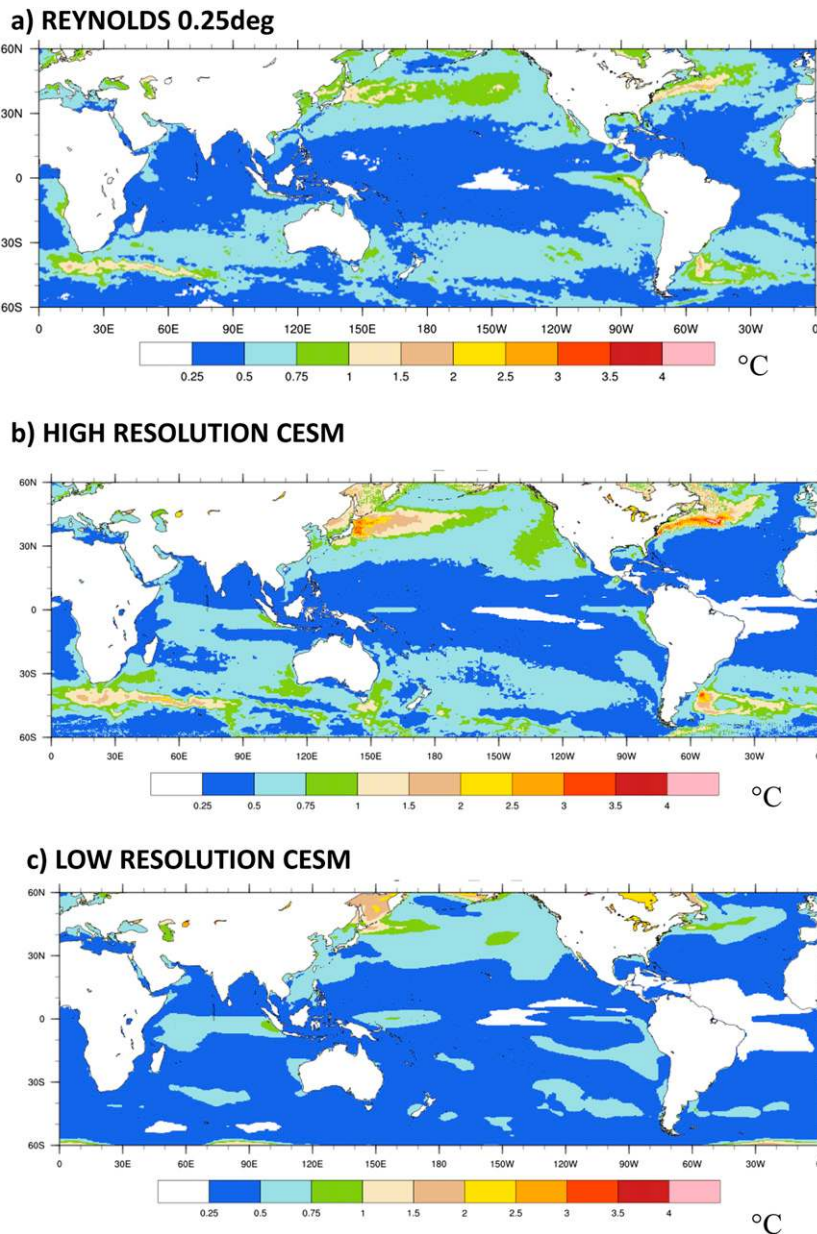


FIG. 1. Standard deviation of monthly anomalies of SST from (a) Reynolds et al. (2007) OISST, (b) CESM-HR, and (c) CESM-LR. The monthly climatology has been removed, as has a regression on Niño-3.4 SST.

the low-resolution model has insufficient variability in those regions and in the Southern Ocean. It may also be noted that both models have too little tropical Atlantic variability.<sup>1</sup>

<sup>1</sup> In addition CESM-LR has high SST variance in some high-latitude regions such as around 60°S, 90°E, and the Sea of Okhotsk and Hudson Bay. This is because the global surface temperature was analyzed, and for CESM-LR, but not CESM-HR and J-OFURO3, surface temperature over sea ice was included.

In the high-variability regions of the WBCs, the standard deviation of SST in CESM-HR is 2–3 times that seen in the OISST product [see also Fig. 18 of Small et al. (2014)].<sup>2</sup> However, caution needs to be taken before concluding that the model SST variability is too

<sup>2</sup> Another high-resolution climate model, the GFDL CM2.6 (Delworth et al. 2012; Griffies et al. 2015), also gives much higher SST variability in the WBCs than OISST.

high, because of the lack of observations in WBCs and the fact that the OISST product has an inherent smoothing over a 50-km radius in these regions (Reynolds et al. 2007). This is expanded upon in section 6a.

Regarding the nature of the SST variability in the high-resolution model and OISST, analysis of daily snapshots and monthly mean data revealed that in WBC regions it is mainly due to a combination of eddies and meanders along the SST fronts (Figs. S5 and S6). On monthly time scales, there is not much smearing of eddy or meander signatures at the latitudes of these fronts. [Propagation speeds of eddies identified by Chelton et al. (2011) are  $\sim 1\text{--}2\text{ cm s}^{-1}$  at latitude  $40^\circ$ , which would be equivalent to  $\sim 26\text{--}52\text{ km month}^{-1}$ , which is less than typical eddy radii at those latitudes.] For that reason we refer to the SST-driven air–sea interactions on monthly time scales as “local.”

Moving on to LHF variability from J-OFURO3 (Fig. 2), it can be seen that in observations the variability is enhanced in WBC regions and to a lesser extent in the subtropical gyres (Fig. 2a). Some similar conclusions regarding model fidelity hold for LHF variability as for the SST variability. CESM-HR has too much variability in WBC regions; for example the standard deviation reaches up to  $70\text{ W m}^{-2}$  in CESM-HR in the North Atlantic but is less than  $50\text{ W m}^{-2}$  in J-OFURO3 (Figs. 2a,b). CESM-LR has high variability off the east coast of the United States and off Asia, but the maxima in CESM-LR are more tied to the land–sea boundary than in the observations and high-resolution model (Fig. 2c). CESM-LR has too weak variability in the Southern Ocean, and both models have weak variability in the tropical Atlantic. The high LHF variability in CESM-HR in WBCs is to be expected; we show below in section 4 that in these regions much of the LHF variability is driven by SST, and it follows that model LHF variability will be too high if its SST variability is also high.

The simultaneous correlation between SST and LHF<sup>3</sup> in J-OFURO3 shows well-defined maxima in the equatorial region and WBC regions, often reaching above 0.7 (Fig. 3). The spatial pattern of correlation in CESM-HR is much closer to observations than in CESM-LR (Figs. 3b,c), although CESM-HR has higher values in the WBCs and Antarctic Circumpolar Current (ACC) compared to observations. In contrast CESM-LR has very weak correlations throughout the extratropics except in small regions off the U.S. East Coast and northern Japan (where the boundary current separates

from the continent at low resolution, farther north than seen in observations and the high-resolution model), and off the southwest tip of Australia.

A comparison of the J-OFURO3 results with other observational analyses is given in Fig. S7. First, when OAFlux was analyzed for the years 1985–2014 [similar to the period used in Bishop et al. (2017)], it gave a qualitatively similar picture to J-OFURO3 but with slightly weaker correlation in WBCs (Fig. S7a). However, when the later satellite era of 2002–12 only was analyzed, when satellite data was more plentiful than in earlier years and which included the AMSR data, it was found that OAFlux, J-OFURO3, and SeaFlux all gave similar results (Figs. S7b,c,d). Of the products, SeaFlux has slightly larger correlations in the interior oceans (Fig. S7d).

A more complete picture of the relationship between SST and air–sea heat fluxes is provided by also analyzing the correlation between SST tendency and heat flux (Kirtman et al. 2012; Bishop et al. 2017). As heat fluxes are defined as positive upward, the sign convention is such that negative values of LHF–SST tendency correlations in Fig. 4 imply that ocean SST responds to surface heat fluxes (i.e., there is cooling of SST when air–sea fluxes drive heat loss from the ocean). Consistent with the above papers we find that the tendency of SST in midlatitudes and subtropics was mainly driven by surface heat fluxes in the low-resolution model (Fig. 4c): in contrast in the high-resolution model (Fig. 4b) and observed product (Fig. 4a), the correlation between SST tendency and heat flux was near zero in WBCs, and throughout most of the extratropics the high-resolution model and observational analyses had a much weaker negative correlation between SST tendency and heat flux than in the low-resolution model (Fig. 4).

### b. Interannual variability

Next, longer time scales (interannual) are examined, using annually averaged data. (For this analysis, years 2002–12 are first analyzed). Maps of the correlation between SST and LHF on this time scale (Fig. 5) show that, in general, for the analyses and both resolutions of the model, the correlation becomes more positive over most of the globe compared to monthly data (Fig. 3). In WBCs the annual correlation often exceeds 0.9 in observations and CESM-HR for interannual variability. However, in some regions the correlation becomes more *negative* (e.g., the subtropical northwest Atlantic, southeast Pacific, and eastern equatorial Indian Ocean in the observational analyses). The area covered by negative correlation is greater in J-OFURO3 than in CESM-HR, where it is mostly limited to the western Pacific and western Atlantic warm pools. As with

<sup>3</sup> In this and all other occurrences, correlations are performed on anomalies, either monthly or interannual.

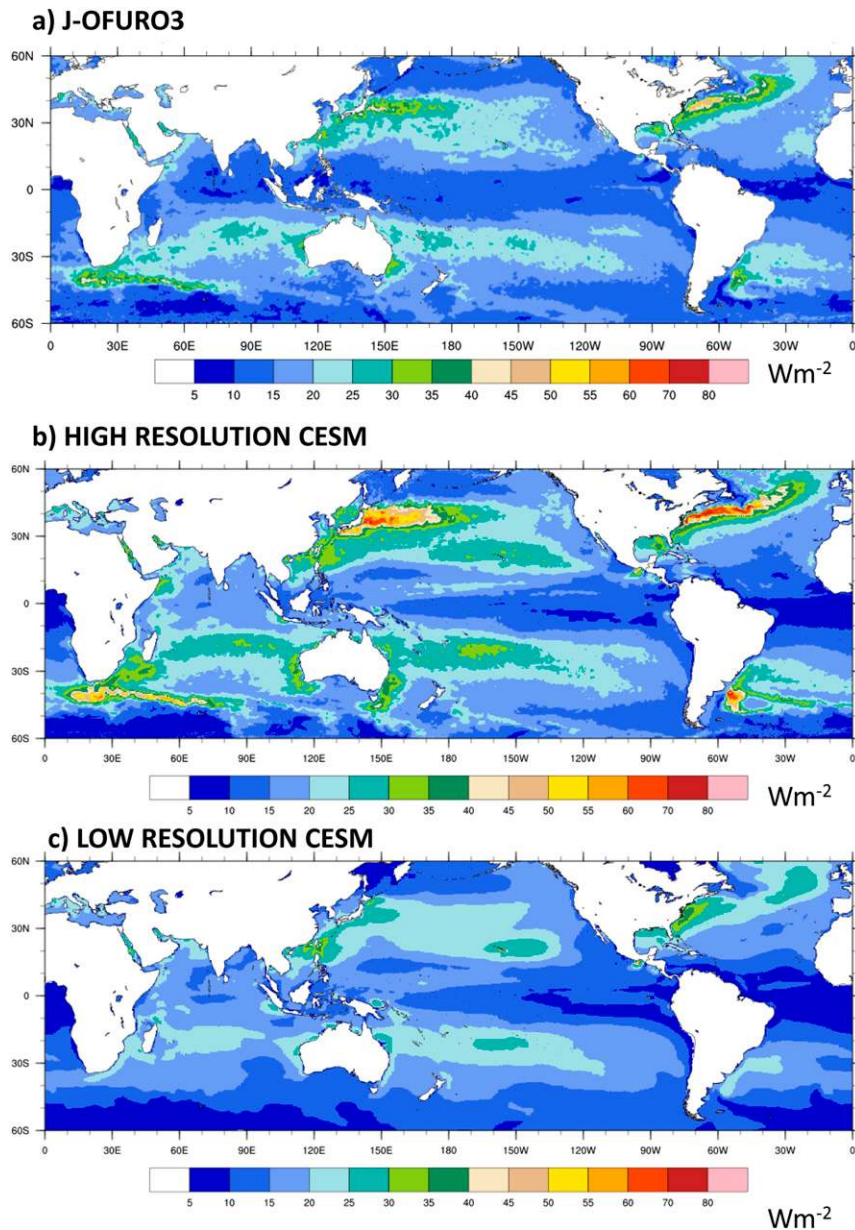


FIG. 2. Standard deviation of monthly anomalies of latent heat flux from (a) J-OFURO3, (b) CESM-HR, and (c) CESM-LR.

the monthly data, CESM-HR typically has somewhat stronger correlations than observed, while CESM-LR is much weaker and still near-zero in many regions of the globe (Fig. 5). Note that unlike the monthly variability, where air–sea interactions are quite local (see section 3a), for interannual time scales the SST anomalies could represent some “smearing out” of propagating eddies, or they could be coherent shifts of ocean fronts and true interannual variability. We do not distinguish between them here but consider the anomalies as intrinsic ocean variability if they drive

surface heat fluxes. (This will be expanded upon in current and future work where the Ekman heat transport anomaly is also considered.)

It may be questioned whether analysis of the limited years 2002–12 is sufficient for interannual variability. We have compared the annual correlations derived from the OAFux record for 1985–2014 with that from 2002–12 (Fig. S8). Although the result from the shorter record is somewhat noisier, as might be expected, it is qualitatively the same as the long record, but with some quantitative difference. Some differences are to be expected



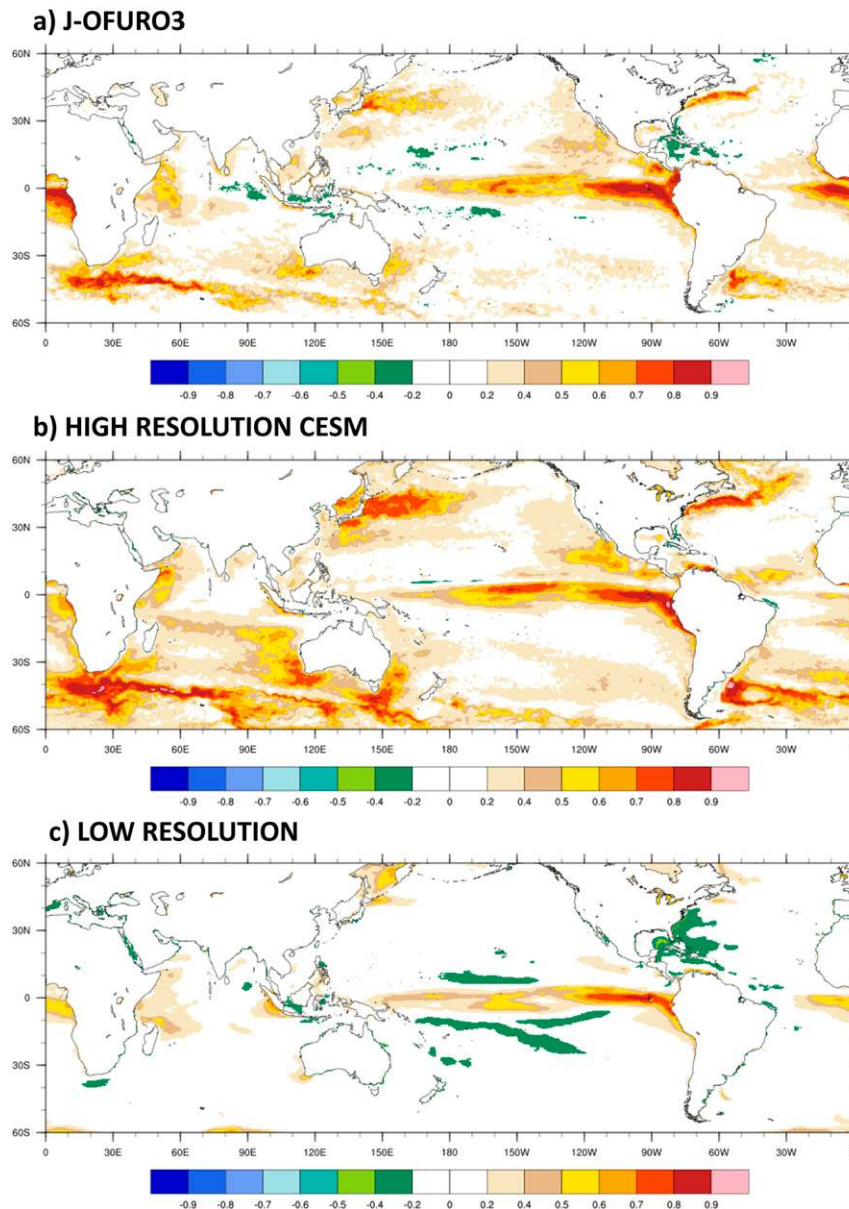


FIG. 3. Correlation between monthly anomalies of latent heat flux and SST from (a) J-OFURO3, (b) CESM-HR, and (c) CESM-LR.

because of the higher availability of data in the 2002–12 period which could lead to the higher correlations seen in the later period (see Fig. S8), as well as natural climate variability.

#### 4. Driving factors of latent heat flux variability

We now turn our attention to the relative roles of SST, wind, and low-level atmosphere thermodynamic state (humidity) in driving the LHF variability using the two methods described in section 2d. Monthly anomalies are

analyzed. The focus is on the observed product J-OFURO3 and the high-resolution model CESM-HR: CESM-LR is not considered in this section as we already know its LHF variability is too much affected by atmosphere processes, especially in, but not limited to, the WBC regions (section 3).

##### a. Method 1: Partial regression technique

The partial regression and correlation method (section 2d) is employed to deal with interactions between forcing variables, such as those evidenced in Fig. S4.

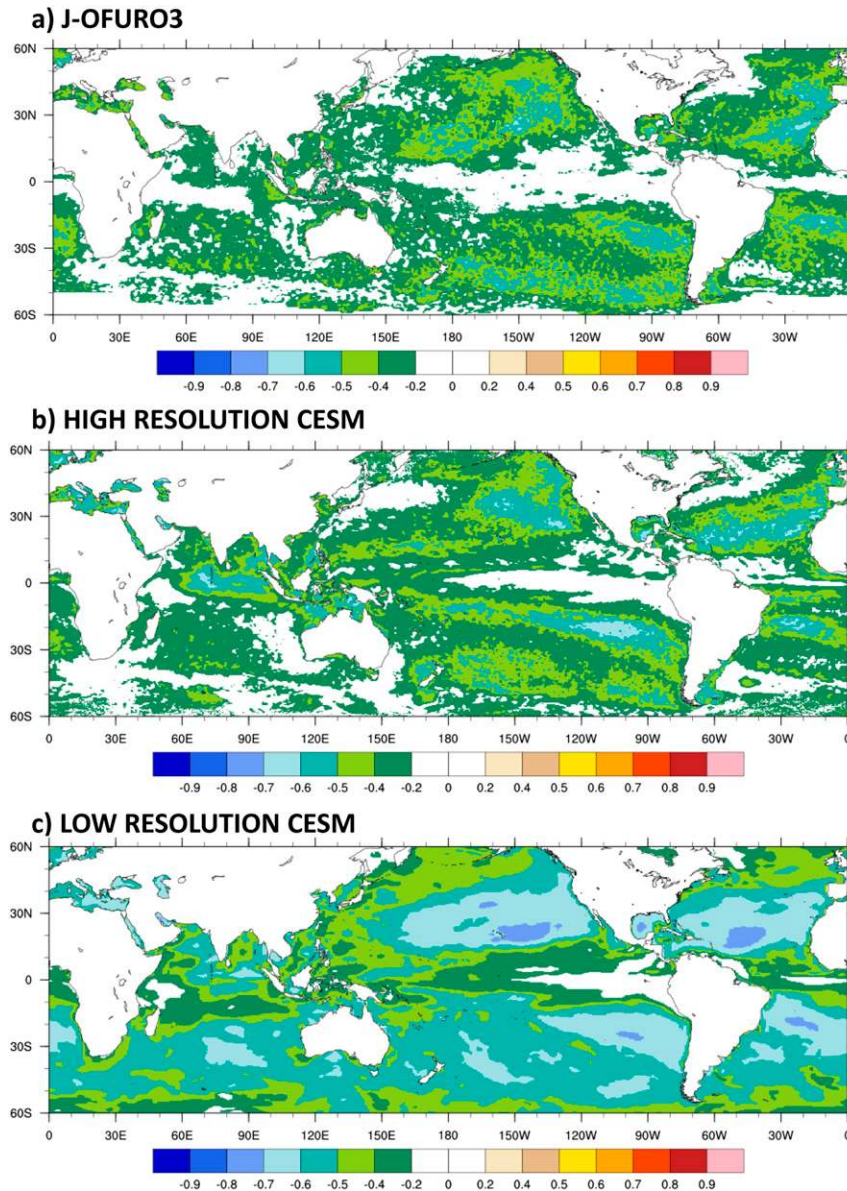


FIG. 4. Correlation between monthly anomalies of latent heat flux and SST tendency from (a) J-OFURO3, (b) CESM-HR, and (c) CESM-LR.

The partial correlation between wind and LHF is always positive, meaning enhanced wind variability is associated with higher heat loss from the ocean and evaporation (Figs. 6a,b). Some of the highest correlations are in subtropical trade wind regions and the extratropical storm tracks, which coincide with the strongest time-mean wind stress regions (not shown). High correlations are also seen in the west Pacific warm pool and equatorial Indian Oceans, which are low time-mean wind speed regions, but there the wind variability can be reasonably high (especially in the equatorial

Indian Ocean; Figs. 7a,b) while SST (Fig. 1) and humidity (Figs. 7c,d) variability are weak there.

Atmospheric humidity and LHF exhibit mostly negative partial correlations (Figs. 6c,d); that is, a drier atmosphere is associated with larger LHF (and evaporation) as the difference  $\Delta q = (q_s - q_a)$  in (1) gets larger.

The standard deviation of the reconstructed LHF array using partial regression [(3a)] is compared with the standard deviation of actual LHF in Figs. 8a and 8b. Generally, the differences are small (magnitude  $< 5 \text{ W m}^{-2}$

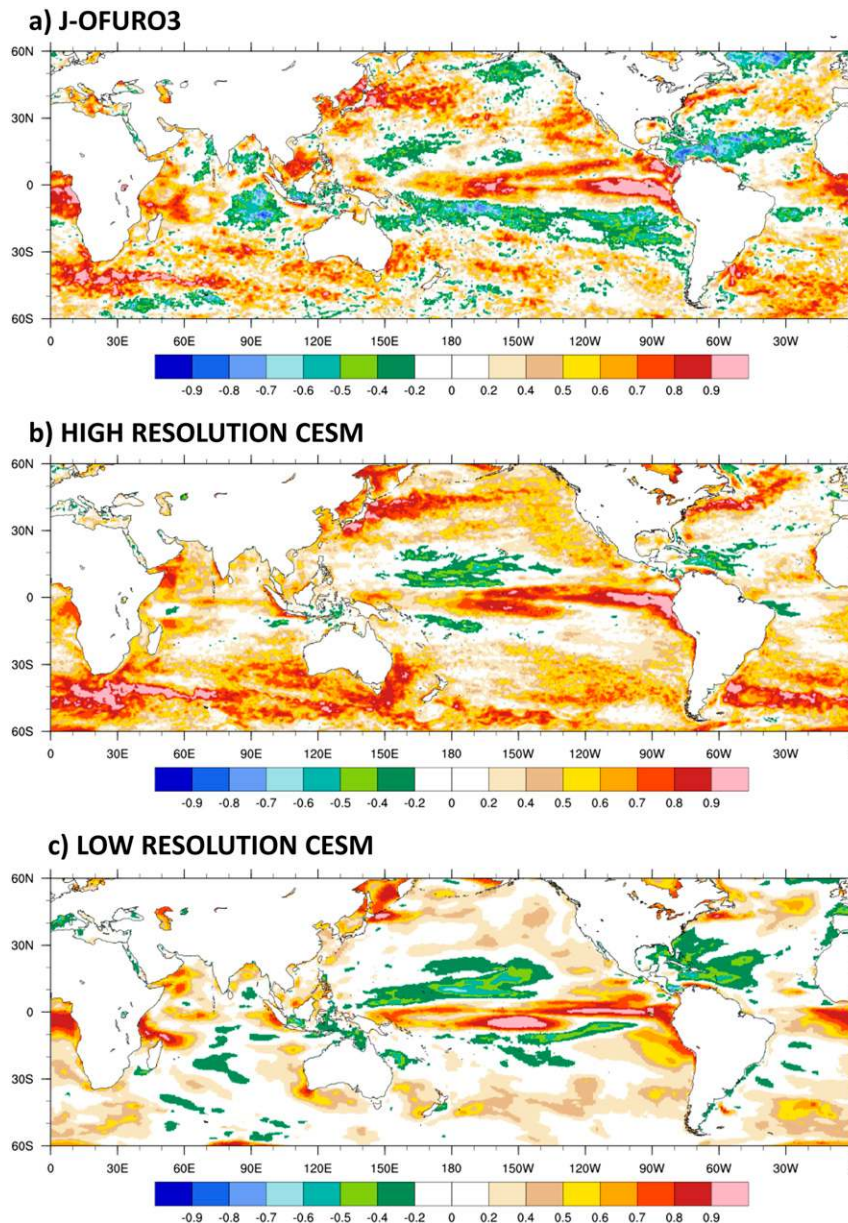


FIG. 5. Correlation between annual anomalies of latent heat flux and SST from (a) J-OFURO3, (b) CESM-HR, and (c) CESM-LR.

in most regions). There still exist some slightly higher differences in WBC regions (up to  $10 \text{ W m}^{-2}$  in CESM-HR), indicating that the partial regression method does not completely remove the interdependence of the state variables, possibly due to nonlinearity.

Another useful metric of the contribution of the state variables is the square of the correlation with LHF, commonly referred to as the  $r^2$  statistic, and listed here as  $r^2(U_a, \text{LHF})$ ,  $r^2(\text{SST}, \text{LHF})$ , and  $r^2(q_a, \text{LHF})$ , and again we are using SST as a proxy for  $q_s$ . As well as

describing the fraction of variance of LHF explained by the state variable, the  $r^2$  statistic can be compared against the results of method 2 as described in section 4c.

The contribution of SST to the LHF variance,  $r^2(\text{SST}, \text{LHF})$ , written as a percentage, is over 50% in much of the WBC regions and eastern equatorial Pacific and Atlantic Oceans in J-OFURO3 and CESM-HR (Figs. 9a,b), with CESM-HR taking larger values as expected from Fig. 3. Outside of these regions, however, the contribution is less than 20%. The low-level wind contribution  $r^2(U, \text{LHF})$  is over 60% in the subtropical

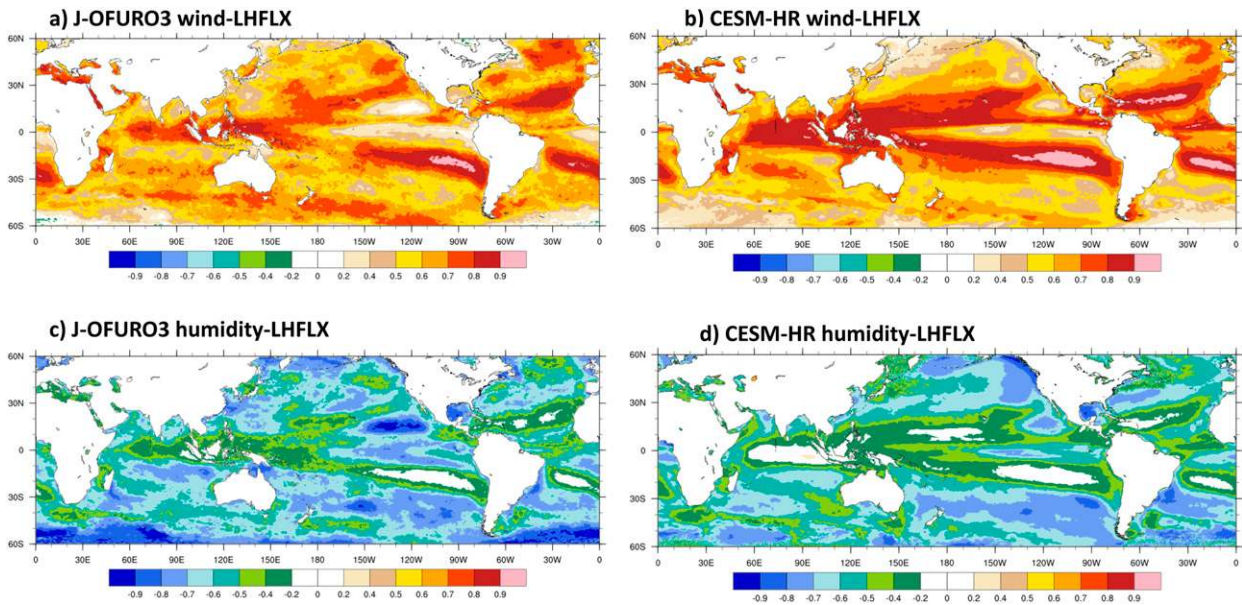


FIG. 6. Partial correlation between monthly anomalies of (a),(b) 10-m wind speed and LHF and (c),(d) 2-m air humidity and LHF for (left) J-OFURO3 and (right) CESM-HR.

trade-wind regions discussed above and over 50% in the tropical warm pools, with again CESM-HR having larger values in these regions (Figs. 9c,d). Atmospheric humidity variability dominates [ $r^2(QA, LHF) > 50\%$ ] in some other regions (Figs. 9e,f), such as poleward of the South Atlantic and southeast Pacific subtropical jets, and in the Gulf of Mexico, at latitudes  $50^\circ$ – $60^\circ$ , and

southeast of Hawaii (the latter most notably in J-OFURO3).

*b. Method 2: Exact decomposition of LHF variability*

As described in section 2d, this method explicitly computes the terms of the LHF decomposition [RHS of (2)], so that they can be directly compared with the full

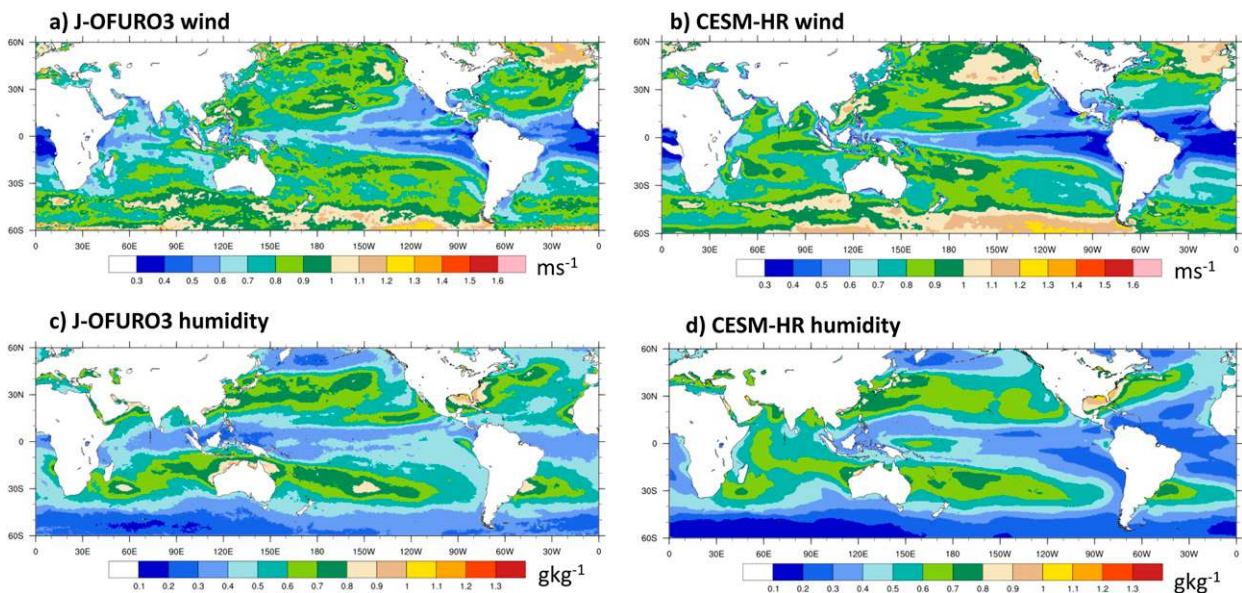
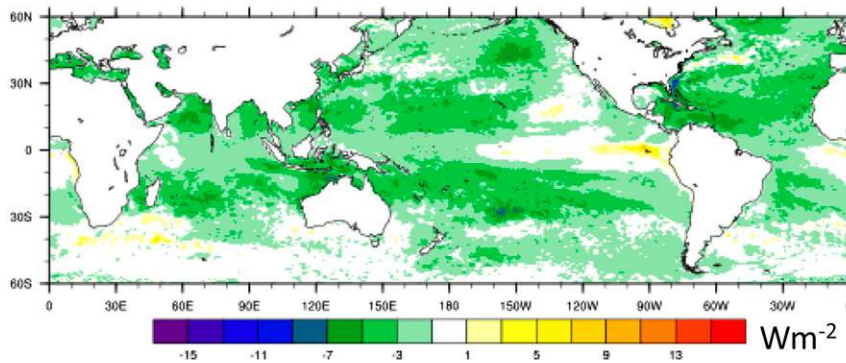


FIG. 7. Standard deviation of monthly anomalies of (a),(b) 10-m wind speed and (c),(d) 2-m air humidity for (left) J-OFURO3 and (right) CESM-HR.

### a) J-OFURO3 partial



### b) CESM-HR partial

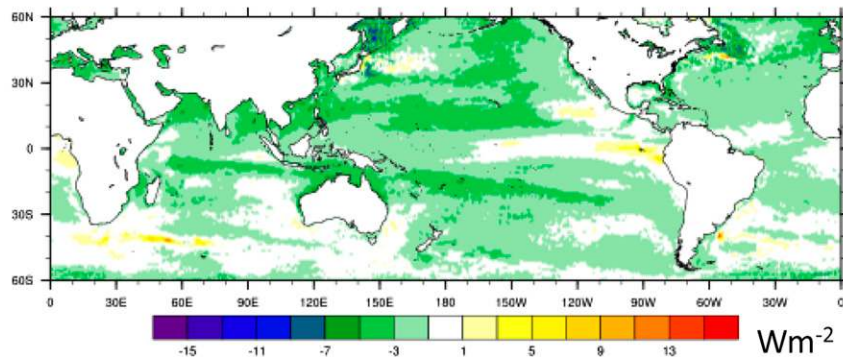


FIG. 8. Differences between the standard deviation of the reconstructed LHF field and the standard deviation of actual LHF using partial linear regression for (a) J-OFURO3 and (b) CESM-HR.

LHF. It does not rely on linear regression/correlation methods to construct the terms: however, for our final assessment of each term we will use a linear regression to compare the variability of each term with that of LHF. It is an alternative method to deal with the problem of dependent variables on the RHS of (2)—a variable may have a high correlation with LHF variability, but if the term in (2) that includes that variable is small, then it is not contributing significantly.

In this subsection we approximate the exchange coefficient  $C_E$  with the climatological monthly mean value of  $C_E$  in (2). The effect of including  $C_E$  variability is discussed in the appendix.

From (2), the wind variability term is multiplied by

$$\rho_a L C_E \Delta \bar{q},$$

while the sea surface and atmospheric humidity variability ( $q_s$  and  $q_a$ , respectively) are multiplied by

$$\pm \rho_a L C_E \bar{U}_a,$$

respectively. Thus the weighting factors both depend on the climatological exchange coefficient, multiplied by the climatological humidity difference and wind speed, respectively. As both the mean wind speed and the mean moisture exchange coefficient are strong in the storm track and monsoon regions (Figs. S9a–d), it follows that the humidity weighting is large there also (Figs. 10b,d). The wind weighting is large in the west Pacific warm pool and Indian Ocean (Figs. 10a,c) and at the Northern Hemisphere western boundaries in boreal winter (Fig. 10a), where air–sea temperature and humidity differences are large (Figs. S9e,f).

The terms of (2) were next regressed on full LHF variability to isolate the parts that are indeed important to LHF (Fig. 11). Here, resulting positive values denote that the term contributes positively to the variability, and a value near 1 denotes dominance of the term; negative values are counteracting. Values greater than 1 are also possible and indicate that another term is compensating. SST (via  $q_s$ ) has a dominant influence in ocean frontal zones and the eastern equatorial Atlantic and Pacific, as expected from section 3 (Fig. 11a), but the

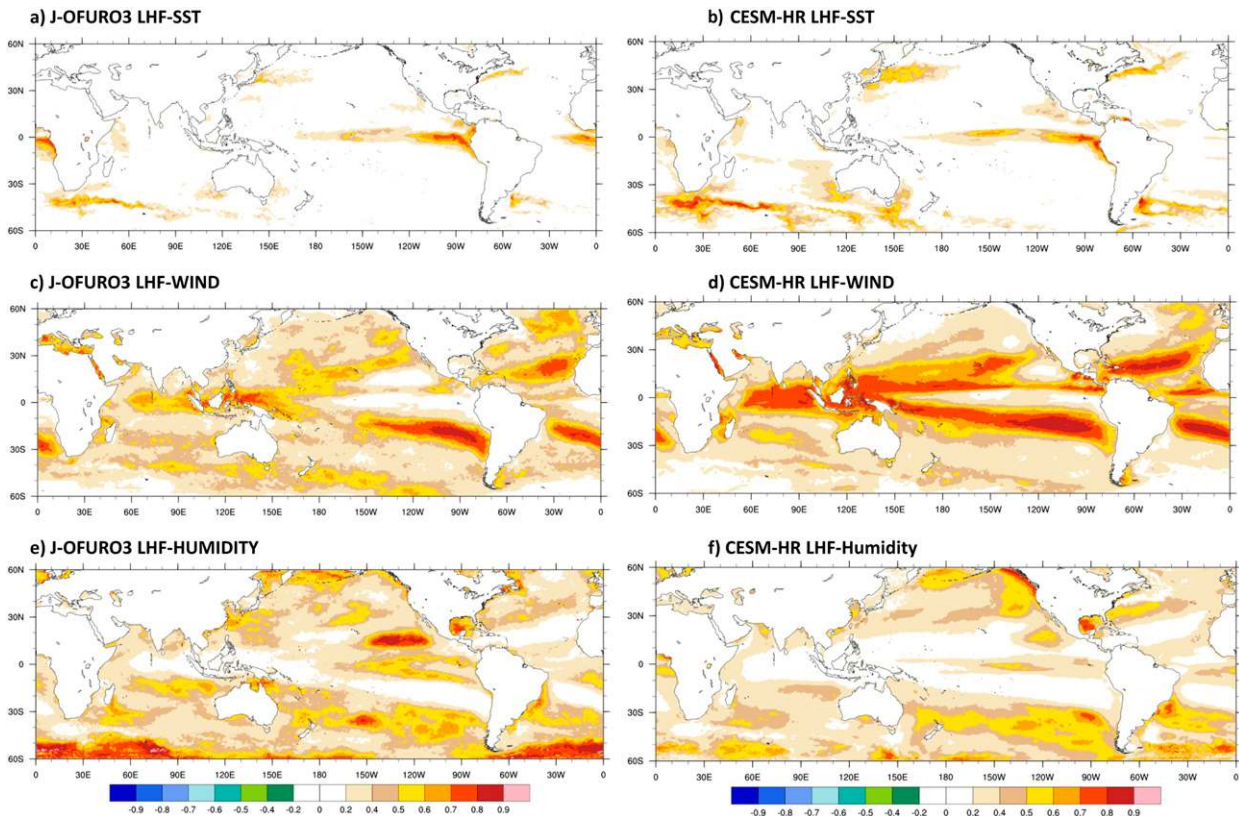


FIG. 9. Square of the correlation ( $r^2$ ) between LHF and driving quantities based on monthly anomalies from (left) J-OFURO3 and (right) CESM-HR: (a),(b)  $r^2(\text{SST}, \text{LHF})$ , (c),(d) partial  $r^2(U, \text{LHF})$ , and (e),(f) partial  $r^2(QA, \text{LHF})$ . All panels share the same color bar shown at bottom.

values are weak elsewhere in the tropics and subtropics away from ocean frontal zones. The wind term dominates in the tropical warm pools and subtropical trade-wind regions (Fig. 11b) but is quite weak in higher latitudes (where the weighting for wind rapidly reduces; Figs. 10a, c), while atmospheric humidity contributes mainly in the higher latitudes (Fig. 11c) where the humidity weighting is large (Figs. 10b,d) and areas such as the Gulf of Mexico where air humidity variability is large (Fig. 7). Note that the wind and air humidity show very weak contribution in the WBC and ACC regions. Note also that in the eastern equatorial Pacific SST reinforces LHF variability but is countered by humidity. When the three terms are combined and then regressed onto LHF variability (Fig. 11d), values between 0.9 and 1.1 are obtained over most of the tropics and subtropics, but drop to between 0.7 and 0.9 farther poleward, and exceed 1.1 in the west Pacific/Indian Ocean warm pool (Fig. 11d). Part of this is due to the exchange coefficient variability discussed in the appendix.

These results confirm that SST variability dominates LHF variability in the eastern equatorial basins and in

ocean frontal zones whereas the wind forces the LHF variability in the subtropics and some regions of the deep tropics, and humidity plays an important role at higher latitudes. Although these results were only obtained for CESM-HR, the similarity of CESM-HR and J-OFURO3 in method 1 would suggest that conclusions derived from the CESM-HR results also apply to J-OFURO3 in method 2 but with a larger contribution of SST variability in WBC in CESM-HR (section 3a).

### c. Interpretation of differences between methods 1 and 2

Close comparison of Figs. 9b, 9d, and 9f ( $r^2$  statistic for partial regression method 1) and Fig. 11 (regression of terms on LHF for method 2) reveals that they are quite similar. This is to be expected: it can be shown that if method 1 is used to formulate a LHF reconstruction [(3a)], which is then regressed on the actual LHF variability, then the contribution of each term (i.e.,  $U_a$ , SST,  $q_a$ ) is given by the correlation squared, that is,  $r^2(U_a, \text{LHF})$ ,  $r^2(\text{SST}, \text{LHF})$ , and  $r^2(q_a, \text{LHF})$ , respectively. In other words, regressing the reconstructed array of method 1 against the

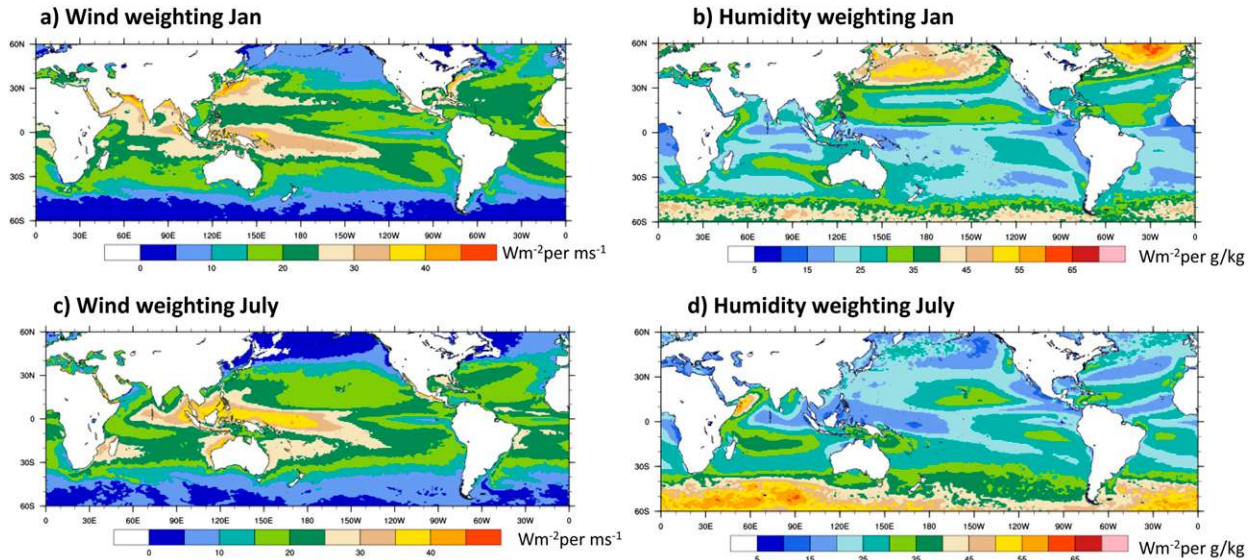


FIG. 10. Weighting factors for LHF variability terms from CESM-HR. Weighting for (left) wind and (right) humidity (atmospheric, when multiplied by  $-1$ , or surface humidity  $q_s$ ). (top) January climatology and (bottom) July.

LHF, and thus trying to mimic method 2 but with estimated weighting, gives a final result of the  $r^2$  statistic, and hence Fig. 11 is comparable to Fig. 9. However, there are some important differences in detail. In Fig. 9, the  $r^2$  values lie between 0 and 1, whereas the results of Fig. 11 cover a larger range (hence the color bar in Fig. 11 is expanded on that of Fig. 9).

In general, the spatial patterns given by methods 1 and 2 are very similar and there are modest differences in magnitude. The quantitative (but not qualitative)

differences are partly due to the fact that the exchange coefficient, and thus the weighting factors, are known exactly in method 2, whereas in method 1 they are estimated, and some variance attributed to state variables in method 1 may in fact be due to variability of the exchange coefficient. Finally, the regression coefficients used in method 1 are constant in time, whereas the weighting functions for method 2 are defined for each month of the calendar year (i.e., monthly climatologies.).

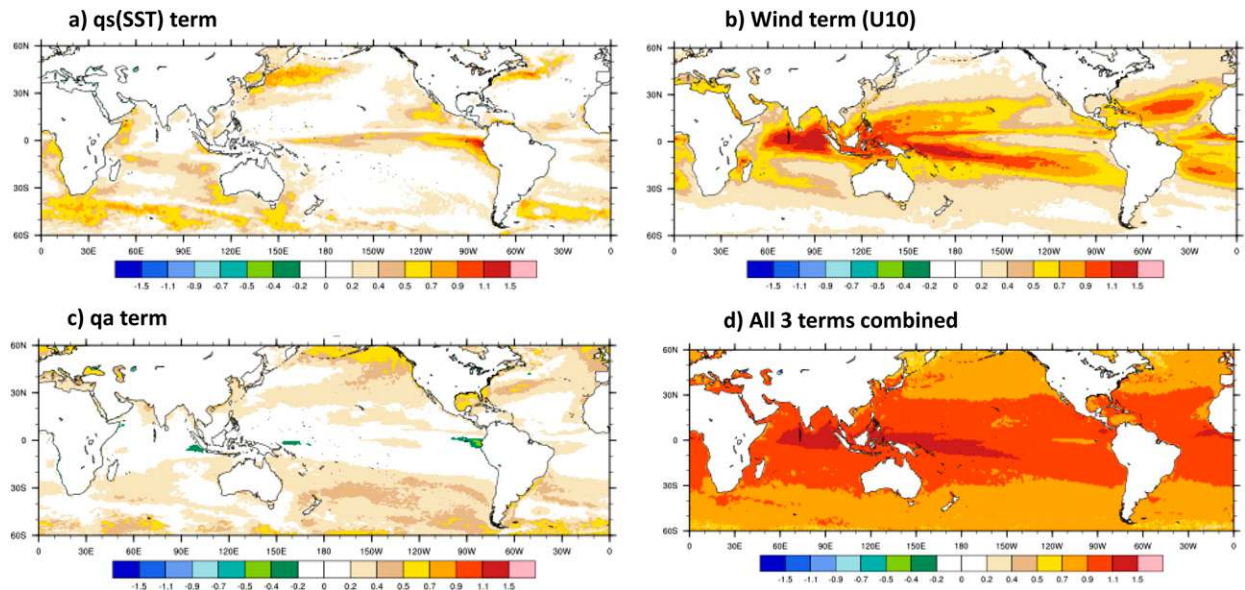


FIG. 11. Linear regression of individual terms of LHF decomposition onto full LHF variability, based on CESM-HR, from method 2: (a)  $q_s$  (SST) contribution, (b) wind contribution, (c) air humidity contribution, and (d) contribution of all three terms. The displayed quantity is unitless.

## 5. Scale dependence in space and time

Here we investigate whether the relationship between SST and the turbulent heat fluxes described in section 3 varies as a function of space and time scale. The aim is to see whether there are particular scales of transition between atmosphere-driven and ocean-driven cases. The observational analyses and high-resolution CESM are considered: CESM-LR is not analyzed as section 3 showed that CESM-LR is erroneously overdominated by the atmosphere forcing at the spatial grid scale and monthly time scale over most of the globe.

### a. Spatial scale dependence

The results so far in this paper are based on local, grid-scale ( $0.25^\circ$ ) relationships. As many previous papers suggest that the ocean mesoscale has an impact on air–sea interaction, it would be useful to see here if the ocean driving of surface turbulent heat fluxes is confined to particular spatial scales. This has been done previously by Bishop et al. (2017), using the OAF flux observed data record, and we here update it to include the higher-resolution J-OFURO3 dataset, as well as the CESM-HR model.

First, the changes in behavior as LHF and SST are coarse-grained from their native grid to retain larger scales are considered, using a boxcar smoother. Global maps of SST–LHF correlation from J-OFURO3 are shown in Fig. S10. For cases where the regression on Niño-3.4 SST is removed, there is a monotonic decrease of SST–LHF correlation with increasing spatial scale (Fig. S10, left column). The most rapid changes are seen between  $1^\circ$  and  $5^\circ$  smoothing. When the regression on Niño-3.4 SST is not removed, the situation is similar except in the tropical Pacific where the pattern of positive correlation at the equator flanked by negative correlation stays robust with spatial scale (Fig. S10, right column). This is indicative of the large-scale nature of El Niño.

The dependence on spatial scale is summarized in Fig. 12 by showing the lagged correlation between SST and turbulent heat flux (THF = LHF + sensible heat flux; results using LHF alone would be similar) as a function of spatial scale at the same WBC locations used in Bishop et al. (2017), for J-OFURO3 (right column) and CESM-HR (left column).

CESM-HR compares more favorably with the J-OFURO3 product than with the OAF flux results described in Bishop et al. (2017, their Fig. 10).<sup>4</sup> The high-resolution model and J-OFURO3 have a positive and

symmetric lagged correlation (ocean-driven SST variability) at small spatial scales (Fig. 12) that transitions to a more asymmetric lagged correlation (atmosphere-driven SST variability) at the longest spatial scales (positive correlation when SST leads and negative correlation when heat flux leads).

To quantify at what spatial scale the system changes from atmosphere-driven to ocean-driven J-OFURO3, a transition length scale was defined following Bishop et al. (2017). Here, for all smoothing scales  $L$  smaller than the transition scale  $L_c$ , the absolute value of the instantaneous correlation between SST and THF is greater than the absolute value of the instantaneous correlation between SST tendency and THF [(5) in Bishop et al. 2017]. In practice this is determined for a given geographical location by fitting a polynomial curve to the correlation values as a function of smoothing scale  $L$ , as seen in Fig. 13. Then the transition scale is where the curves for SST–THF correlation (solid lines in Fig. 13) and those for  $\partial\text{SST}/\partial t$ –THF correlation (dashed lines in Fig. 13) intersect.

The transition from ocean-driven to atmosphere-driven SST variability in the WBC regions is between  $4^\circ$  and  $7^\circ$  for CESM-HR and J-OFURO3 (Fig. 13) compared to the  $1^\circ$ – $3^\circ$  range found for OAF flux in Bishop et al. (2017). Resolution improvement and updates to data input in J-OFURO3 compared to OAF flux may be one of the reasons for the differences in transition length scales between products, but a detailed analysis comparing the two products is not done here.

Next, we analyze the correlations between SST and LHF found at small spatial scales. This is done by removing a simple boxcar average of full-width  $5^\circ$  of the original  $0.25^\circ$  data. The resultant high-pass data show very strong instantaneous correlations between SST and LHF in the J-OFURO3 and CESM-HR datasets (Figs. 14a,b), reaching values of 0.8 or more over much of the globe, especially away from the tropics. As with the unfiltered data, CESM-HR exhibits higher correlations, but clearly the high-resolution model and analysis product show fundamentally the same behavior. The weaker correlation in the tropics in the high-pass data compared to unfiltered data may be due to less small-scale ocean activity compared to the extratropics, combined with forcing of heat fluxes by small-scale convective systems such as that embedded in the Madden–Julian oscillation (MJO; Madden and Julian 1994). The fact that the SST–LHF correlation away from WBCs is much weaker when the data are unfiltered (Figs. 3a,b) than for high-pass filtered (Figs. 14a,b) reveals that in those regions ocean eddies are present and force modification of the heat fluxes, but this is overwhelmed by larger-scale atmosphere forcing. In contrast,

<sup>4</sup> Following the results shown in section 3a and Fig. S7, part of this may be due to the longer time period analyzed in Bishop et al. (2017), 1985–2013, the earlier part of which tended to weight the SST–LHF correlation toward smaller values.



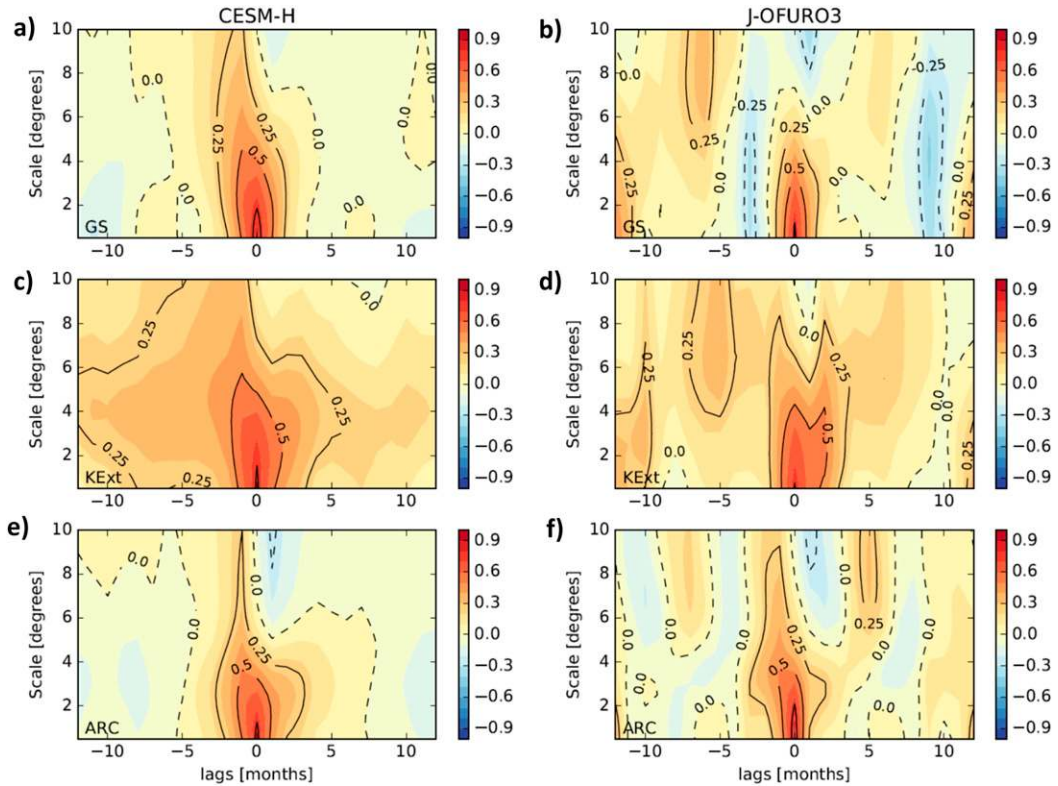


FIG. 12. Scale dependence. Sensitivity of the lag covariance function between SST and THF to spatial scale of smoothing (ordinate) for (left) CESM-HR and (right) J-OFURO3 in (a),(b) the Gulf Stream (GS), (c),(d) the Kuroshio Extension (KExt), and (e),(f) the Agulhas Return Current (ARC). Negative (positive) lags denote SST (LHF) leads. Exact locations are shown in [Bishop et al. \(2017\)](#).

within the WBCs, the small-scale ocean features are strong enough to dominate the heat flux variability.

*b. Temporal scale dependence*

In addition to the role of spatial extent in air–sea interaction, there is an expected dependence on time scale,

with, for example, atmosphere weather systems likely to have a large influence on heat fluxes at synoptic time scales. [Bishop et al. \(2017\)](#) explored time dependence in the OAFflux dataset but did not go to frequencies higher than monthly. Here we expand this analysis and address time scales from daily to interannual using OAFflux. Daily

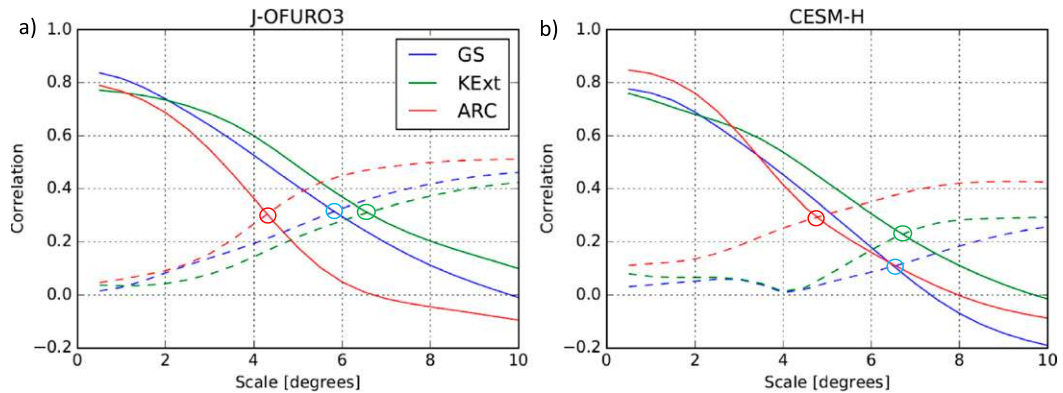


FIG. 13. Transition length scale based on the [Bishop et al. \(2017\)](#) methodology for (a) J-OFURO3 and (b) CESM-HR. Solid lines are the instantaneous correlation between SST and THF at a particular location as a function of spatial scale from [Fig. 12](#); dashed lines are similar but for instantaneous correlation between SST tendency and THF. Different colors denote different locations (see legend). The transition scale is defined as the scale at which the solid and dashed lines of a particular color intersect, as circled.

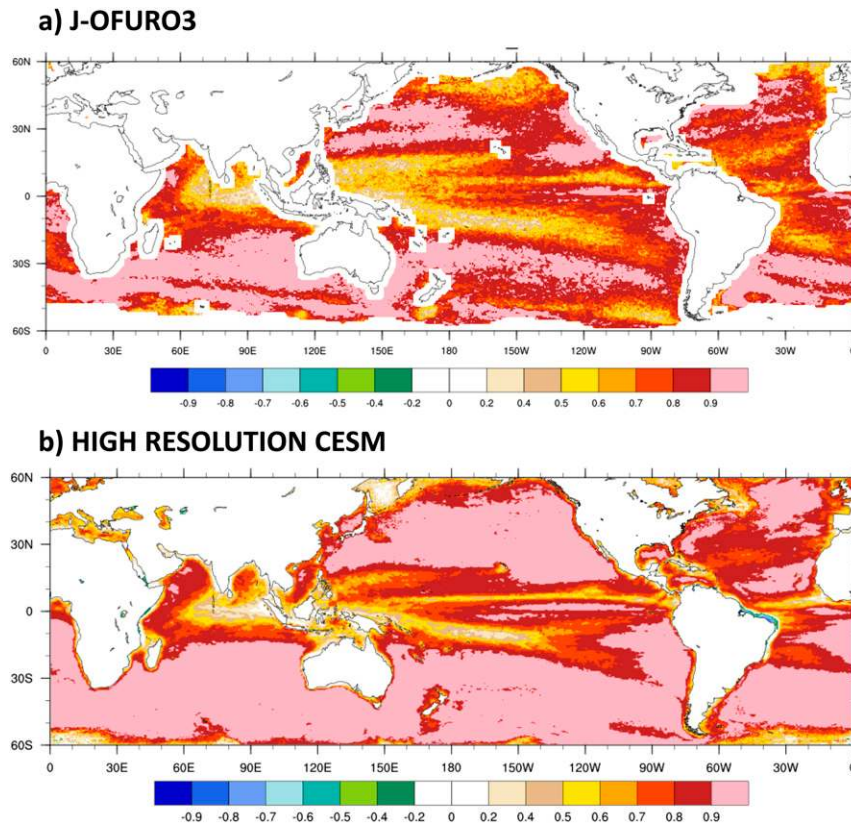


FIG. 14. Correlation between monthly anomalies of SST and LHF, where the data from (a) J-OFURO3 and (b) CESM-HR are high-pass filtered to retain scales of  $\sim 500$  km or less (by removing the boxcar average over 500-km full-width).

anomalies are defined as relative to a monthly climatology (an alternative method of defining a daily climatology gave similar results). Results from the full daily data are then compared with those from the daily data smoothed with a fourth-order Butterworth low-pass filter with cutoffs of 5, 10, 30, 180, and 365 days, referred to as  $n_{\text{day}}$  here.

The temporal dependence is illustrated for the northwest Pacific in Fig. 15 (results for the northwest Atlantic are shown in Fig. S11). For the unfiltered daily data and  $n_{\text{day}} = 5$ , the correlation between SST and THF is weak and lies between 0 and 0.3 (Figs. 15a,b), with the largest values along the Kuroshio Extension, indicative of a mainly atmosphere-driven regime under synoptic storms with a small influence of the ocean variability. The positive correlation mostly increases monotonically with smoothing scale; for  $n_{\text{day}} = 30$  it reaches up to 0.5 (Fig. 15c) and for  $n_{\text{day}} = 180$  and 365 there is a broad expanse of strong correlation values ranging from 0.4 to 0.8 (Figs. 15c,d). (Results for the northwest Atlantic are somewhat similar but with generally lower correlation, including some negative correlation outside of the WBCs; see Fig. S11.)

Regarding the time dependence of SST–LHF relationships in the high-resolution climate model, inspection of an animation of LHF over SST from hourly data of CESM-HR<sup>5</sup> reveals the dominance of weather systems in driving LHF at the submonthly time scales in mid-latitudes, most notably cold-air outbreaks off the east coast of the Northern Hemisphere continents and synoptic storms in the Southern Ocean that bring cold and dry air from high latitudes toward the equator. However it also reveals the collocation of some of the strongest LHF in these events with warm meanders of the WBCs and ACC, indicative of the role of the ocean that becomes more dominant at longer time scales (section 3).

## 6. Discussion

### a. SST variability

In section 3a it was shown that CESM-HR had much larger SST variance than a  $0.25^\circ$  analysis of SST

<sup>5</sup> See the video at [https://www.youtube.com/playlist?list=PL5BdpELeiG4Boo-JCGr\\_34WmnNf9tt4wn](https://www.youtube.com/playlist?list=PL5BdpELeiG4Boo-JCGr_34WmnNf9tt4wn).

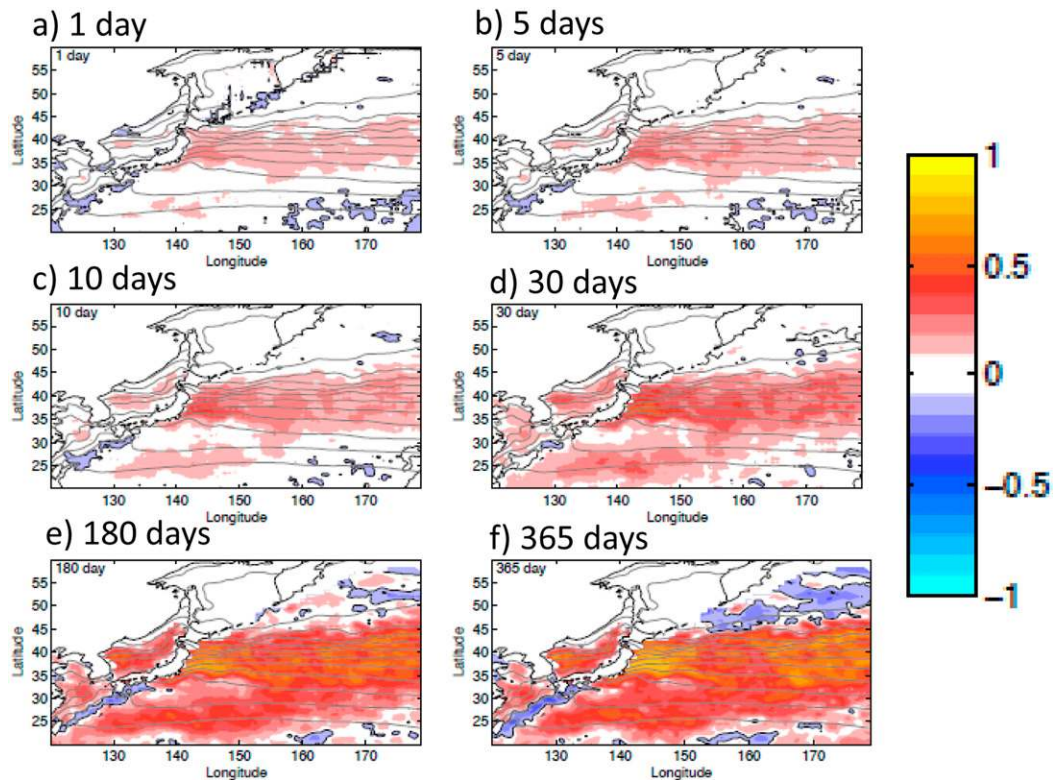


FIG. 15. The correlation of SST and turbulent heat flux in the northwest Pacific for different time scales. Data are from the OAFflux (Yu and Weller 2007) product. The data are low-pass filtered for the number of days labeled at the top of each plot (see text for details). The climatological annual cycle is removed, as is regression on Niño-3.4 SST.

(OISST), especially in WBCs. It has previously been shown that OISST exhibits less SST variability on sub-monthly time scales than U.S. National Data Buoy Center East Coast buoys (Reynolds and Chelton 2010), and when compared to Climate Variability and Predictability (CLIVAR) Mode Water Dynamics Experiment (CLIMODE; Marshall et al. 2009) data (Jin and Yu 2013), but the comparisons for monthly and longer variability are less clear due to shortness of buoy records. Note that SST products with much higher resolution than OISST and with less smoothing do exist (Donlon et al. 2007; Martin et al. 2012) but, as described by Reynolds et al. (2013), these products have severely limited data sources in the low cloud regime of the Gulf Stream and Kuroshio, especially in winter, when AVHRR coverage is scarce. (They showed that for a typical month of January, there were less than 3 days when there were at least 50% of cloud-free pixels in the Gulf Stream and Kuroshio region, and only 15 days in July, while in the Southern Ocean the coverage was poor year-round).

In an evaluation of one high-resolution (1 km) SST dataset, which uses an analysis of SST tailored to the resolution of the available satellite data [known as the NASA Jet Propulsion Laboratory Multiscale Ultrahigh

Resolution (JPL-MUR) product], Chin et al. (2017) showed that, globally, older products such as the OISST had severely limited spectral power density of SST in the below  $\sim 200$ -km wavelength range, compared to infrared satellite data. Specifically, the wavenumber  $k$  power spectra of high-resolution satellite SST (such as from the MODIS *Terra* instrument) showed an approximate  $k^{-2}$  slope (i.e.,  $SST^2 \sim k^{-2}$ ), whereas the OISST and many similar products dropped off rapidly from this slope in the below  $\sim 200$ -km wavelength range. The JPL-MUR product had much higher spectral power density globally in this range of spatial scales; however, for most of the regions of focus of this paper it is still severely limited by the extent of cloud cover, and hence we do not use it here.

Laurindo et al. (2018) have also suggested high SST variance in a high-resolution climate model with the same resolution ocean model as in CESM-HR, but using  $0.5^\circ$  CAM4 (Kirtman et al. 2012). This was inferred from the fact that the anomalies of wind speed driven by SST had too high variance (compared to satellite data). However, power spectral density of SST from this high-resolution simulation had spectral slopes of around  $k^{-2}$  (L. Laurindo 2018, personal communication), similar to that found by Chin et al. (2017) for high-resolution

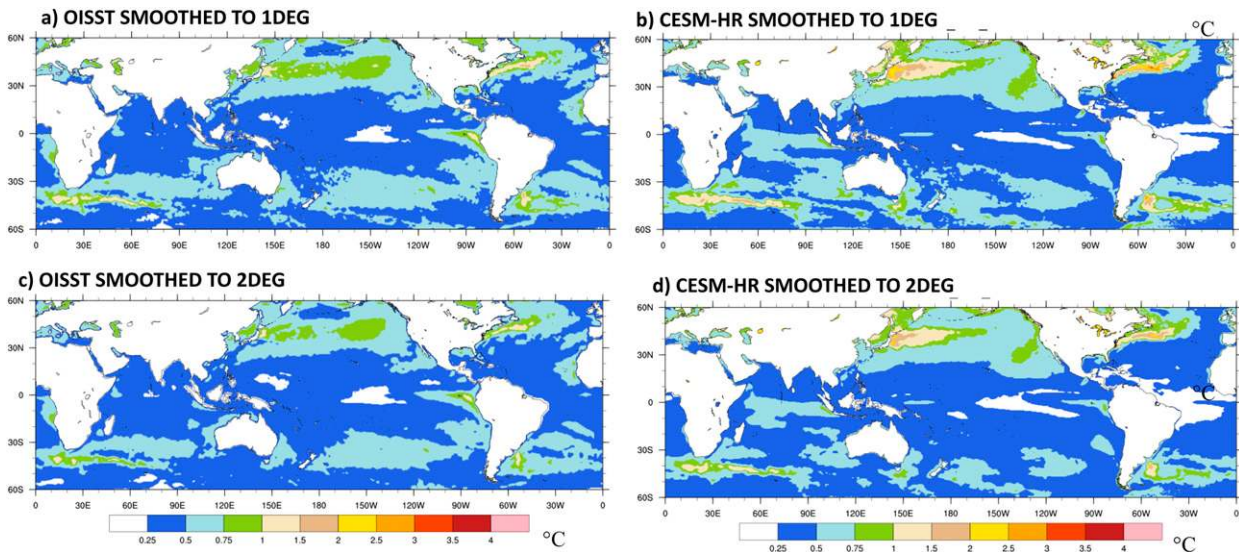


FIG. 16. Standard deviation of monthly anomalies of SST, with spatial smoothing: boxcar smoothing full width  $1^\circ$  for (a) OISST and (b) CESM-HR, and boxcar smoothing full width  $2^\circ$  for (c) OISST and (d) CESM-HR.

satellite data, and again with much higher variance at small wavenumbers than OISST.

To confirm whether the high SST variance in CESM-HR is due to small-scale motions we repeat the calculations used for Figs. 1a and 1b but using spatially smoothed data. When the data are smoothed with a boxcar running average of full-width  $1^\circ$ , the standard deviation of OISST is hardly affected (cf. Fig. 1a and Fig. 16a) but for CESM-HR it is significantly reduced (Fig. 1b and 16b). Next, smoothing with a  $2^\circ$  boxcar average does lead to some reduction of the standard deviation of OISST in WBCs (Figs. 1a and 16c) while CESM-HR is brought quite close to the original OISST standard deviation (cf. Figs. 1a and 16d). Therefore the results confirm that much of the excess SST variance in CESM-HR is at scales of  $2^\circ$  or less (which are not well captured by OISST and similar datasets), and additionally that OISST does not capture much variability at scales of  $1^\circ$  or less, as expected due to the inherent smoothing in the OISST analysis procedure.

### b. Transition scale

The transition scale (between atmosphere-driving and ocean-driving) defined in this paper identifies the intersection of the SST-LHF and  $\partial\text{SST}/\partial t$ -LHF curves as a function of smoothing scale. The scale of SST anomalies was identified as between  $4^\circ$  and  $7^\circ$  in both J-OFURO3 and CESM-HR, and we assign approximate wavelengths of SST anomalies as being twice these values, thus  $8^\circ$ – $14^\circ$ . The results are somewhat consistent with recent findings of Laurindo et al. (2018) that the phase difference between SST and low-level wind speed

transitioned at zonal wavelengths close to the atmospheric first baroclinic Rossby radius of deformation, which ranges from about 1000 km at  $40^\circ$  latitude to 2500 km at the equator. (When considering SST–wind speed relationships, the ocean-driven case has a phase difference of close to  $0^\circ$ , while the atmosphere-driven case is close to  $180^\circ$ ).

These transition scales are much larger than the first internal Rossby radius of deformation of the ocean, which is  $O(10)$  km in the extratropics and a maximum of around 250 km at the equator (Chelton and deSzoeke 1998). However Laurindo et al. (2018) also noticed that the squared coherency (a quantity related to correlation but defined in spectral space) between SST and wind speed peaked at a zonal wavelength around 4 times the observed radius of eddies  $r_o$  [determined from satellite data by Chelton et al. (2011)]. The latter scale of  $4r_o$  can be considered as approximately equivalent to a wavelength of meanders on a front. The implication is that the atmosphere-driving case mainly occurs at spatial scales larger than the atmosphere Rossby radius: below that scale the situation is ocean-driven with peak forcing at the ocean eddy scale.

### c. Effect of small-scale heat fluxes on large scale

It may be asked whether the small-scale intrinsic variability described in this paper has a significant effect on the time-mean heat fluxes and/or on larger-scale variability. These are not easily addressed in the modeling framework of this paper: the CESM-HR and CESM-LR have very different mean surface heat fluxes in regions such as the Gulf Stream and North Atlantic

Current [as found in another coupled model by Roberts et al. (2016)], but much of this is due to the different paths of the mean current and the direct effect of eddies on the mean heat flux is not clear. The regional atmosphere model experiments presented in Ma et al. (2017) were more appropriate for this question: twin experiments were run, one with realistic SST and one with spatial smoothing applied to the SST. In the latter the SST used to compute fluxes was smoothed sufficiently to remove the eddy structures but left the mean ocean circulation and SST fronts mostly unchanged. In their case, they argued that the mesoscale SST affected the atmosphere via enhanced diabatic heating in storms, attributing this to the nonlinear dependence of saturation vapor pressure on temperature (Clausius–Clapeyron relationship) with warm eddies having a larger effect. This led to changes in the storm track and a downstream influence on large-scale atmospheric circulation. Smirnov et al. (2015) had previously noted that a stationary warm SST anomaly in the Kuroshio Extension region could lead to changes in local transient eddy fluxes in the atmosphere, balancing the diabatic heating induced by the SST anomaly, leading to deep ascent, and a downstream response.

The role of coherent changes in ocean eddy activity in the Kuroshio Extension on atmosphere heat transport has been explored by Bishop et al. (2015) and references therein. They noted that between years of active eddy activity (unstable state) and weak eddy activity (stable state) a partial compensation between changes in meridional heat transport in the ocean and in the atmosphere was achieved.

The feedback of the small-scale air–sea fluxes to the ocean was investigated by Ma et al. (2016) using coupled high-resolution experiments. They showed that the small-scale air–sea interaction had an impact on the eddying and mean flow associated with the Kuroshio Extension. When the mesoscale air–sea feedback was removed, ocean eddies became more energetic and the flow more meandering with a weak mean ocean jet. In contrast, with realistic feedback and damping of ocean eddies, it was proposed that a strong ocean jet is required to convert mean available potential energy (PE) to eddy PE to balance the strong dissipation of eddy PE by air–sea flux. Further work is required, however, to see if this process acts generally in other regions of the globe and on what time scales.

## 7. Conclusions

- Observational analyses and high-resolution climate models show that LHF variability is driven by SST variability in regions of intrinsic ocean variability on monthly time scales.

- Correlations between SST and LHF generally increase for interannual time scales in those same regions, compared to monthly.
- Standard-resolution climate models miss most of the ocean effect on LHF in the extratropics, and instead LHF variability is driven by atmosphere there.
- Two methods of decomposing LHF variability were explored. First partial regressions were used to deal with interdependency of forcing variables. Second, an exact decomposition of LHF, including exchange coefficient, confirmed that while SST variability drives LHF variability in the eastern equatorial basins and ocean frontal zones, wind variability drives most of the LHF variability elsewhere in the tropics and subtropics, and humidity played a large role at higher latitudes.
- High-resolution CESM has too strong SST variability in WBC regions, compared to Reynolds et al. (2007) OISST, and consequently LHF variability is also too strong. However, much of the extra SST variability in CESM-HR is at scales of  $\sim 200$  km or less and other studies have indicated that OISST and similar products underestimate variability at those scales.
- In regions of strong ocean intrinsic variability, it is found that spatially smoothing the J-OFURO3 and CESM-HR data to scales of  $4^{\circ}$ – $7^{\circ}$  is enough to transition from the ocean-driving to the atmosphere-driving case. These transition scales are longer than the scales of around  $3^{\circ}$  derived from OAFlux in Bishop et al. (2017).
- When the data are filtered to retain only the ocean small scales, of  $5^{\circ}$  or less, a dominance of ocean forcing of heat flux is seen in most of the extratropics in J-OFURO3 and CESM-HR. In the tropics, particularly the west Pacific/Indian Ocean warm pool, the atmosphere can still dominate at small scales.
- For the metric of correlation between SST and LHF on monthly time scales, all three observational analyses considered here, J-OFURO3, OAFlux, and SeaFlux gave similar results for the recent period of 2002–12.

*Acknowledgments.* This project was supported by NASA Physical Oceanography Awards NNX16AH60G and 80NSSC18K0769. The computer simulations were previously performed at the NCAR–University of Wyoming Supercomputer Center and supported by DOE Scientific Discovery for Advanced Computing (SCIDAC) Award SC0006743. OAFlux data were gathered from <http://oafux.whoi.edu/data.html>, and Lisan Yu is gratefully acknowledged for access and discussion of data. J-OFURO3 data were accessed from <ftp://j-ofuro.scc.u-tokai.ac.jp/J-OFURO3>. Hiroyuki Tomita and Masahisa Kubota are thanked for answering

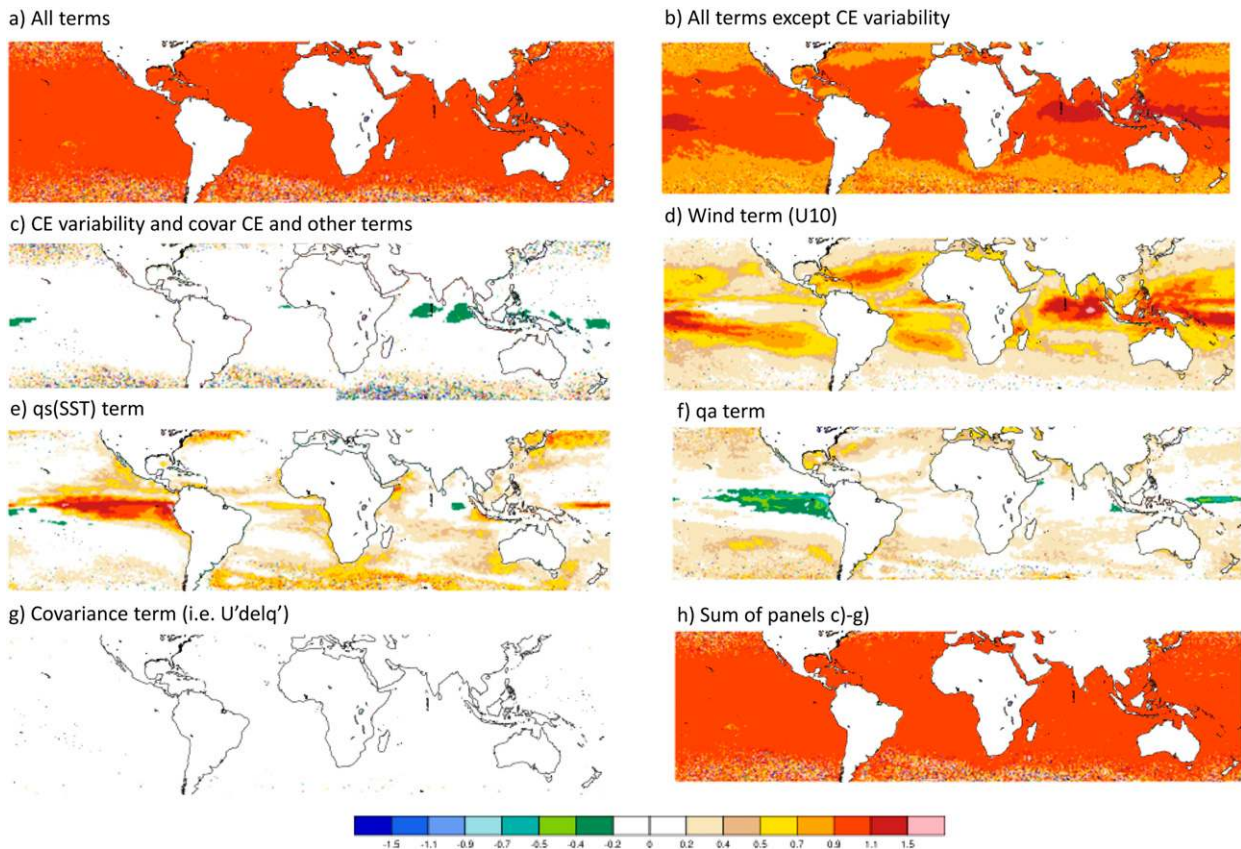


FIG. A1. Linear regression of individual terms of LHF decomposition onto full LHF variability. (a) All terms from RHS of (A1), (b) term i on RHS of (A1), (c) last three terms on RHS of (A1), (d) wind contribution, term iii of (2), (e) term i of (2), (f) term ii of (2), (g) term iv of (2), and (h) sum of (c)–(g), which, by design should be equal to (a). In (d)–(g), it is assumed the exchange coefficient is climatological in (2). Noisy values in the Southern Ocean and high northern latitudes are due to poor estimates of  $C_E$  from daily data in atmosphere storm tracks. The displayed quantity is unitless, and the color bar is shown at bottom.

questions about the dataset. Monthly averaged SeaFlux data were obtained from J. Brent Roberts, who is also thanked for extensive discussion of the data. OISST was gathered from <https://www.ncei.noaa.gov/data/sea-surface-temperature-optimum-interpolation/access/>. CESM-HR data are available at <https://www.earthsystemgrid.org/dataset/ucar.cgd.asd.output.html>. M. Alexander, M. Cronin and C. Gentemann are thanked for discussion of SST and heat flux variability, and L. Laurindo for discussion of spectral decomposition of air–sea interaction metrics and comments on the manuscript. Three anonymous reviewers are thanked for their constructive contribution. F. O. Bryan was supported by the National Science Foundation through their sponsorship of NCAR. The CESM project is supported primarily by the National Science Foundation (NSF). This material is based upon work supported by the National Center for Atmospheric Research, which is a major facility sponsored by the NSF under Cooperative Agreement 1852977.

## APPENDIX

### Effect of Variability of Exchange Coefficient for Moisture on LHF

This appendix studies the effect of variability of the exchange coefficient  $C_E$  on the LHF variability (method 2). If  $C_E$  is divided into climatological mean and perturbation parts as with the other variables, the decomposition (2) is modified to

$$Q'_E = \rho_a L \left( \underbrace{\overline{C'_E A'}}_{(i)} + \underbrace{C'_E \overline{A}}_{(ii)} + \underbrace{C'_E A'}_{(iii)} - \underbrace{\overline{C'_E A'}}_{(iv)} \right), \quad (\text{A1})$$

where  $A$  is the sum of terms in the curly bracket of (2)—that is, terms including wind,  $q_s$ , and  $q_a$  variability and covariability. This decomposition was applied to the 10-yr

record where daily  $C_E$  could be estimated, and note the effects of ENSO were not removed for this analysis. As mentioned in section 2d, estimates of  $C_E$  were very noisy in some storm track regions because the estimate was based on daily-mean data and subdaily variability is strong in storm track regions. Thus, the terms involving the  $C_E$  variability [last three terms of (A1)] are quite noisy in the same regions. This is illustrated in Fig. A1c, where these three terms were regressed onto LHF variability. As a consequence, regressing all four terms in (A1) onto LHF gave noisy values in the same regions (Fig. A1a). When the  $C_E$  variability terms are removed and only the first term of (A1) is used, the fit to the full LHF variability is reduced somewhat from close to 1 in the tropics to 0.7–0.9 in the storm track regions (Fig. A1b).

Because of the noise in the  $C_E$  variability term, we use the smoothed climatological mean  $C_E$  in section 4b, but note that this slightly reduces the fit of the decomposition to the full LHF variability.

#### REFERENCES

- Alexander, M. A., and J. D. Scott, 1997: Surface flux variability over the North Pacific and North Atlantic Oceans. *J. Climate*, **10**, 2963–2978, [https://doi.org/10.1175/1520-0442\(1997\)010<2963:SFVOTN>2.0.CO;2](https://doi.org/10.1175/1520-0442(1997)010<2963:SFVOTN>2.0.CO;2).
- Andreas, E. L., R. E. Jordan, L. Mahrt, and D. Vickers, 2013: Estimating the Bowen ratio over the open and ice-covered ocean. *J. Geophys. Res. Oceans*, **118**, 4334–4345, <https://doi.org/10.1002/jgrc.20295>.
- Barsugli, J. J., and D. S. Battisti, 1998: The basic effects of atmosphere–ocean thermal coupling on midlatitude variability. *J. Atmos. Sci.*, **55**, 477–493, [https://doi.org/10.1175/1520-0469\(1998\)055<0477:TBEAOA>2.0.CO;2](https://doi.org/10.1175/1520-0469(1998)055<0477:TBEAOA>2.0.CO;2).
- Bishop, S. P., F. O. Bryan, and R. J. Small, 2015: Bjerknes-like compensation in the wintertime North Pacific. *J. Phys. Oceanogr.*, **45**, 1339–1354, <https://doi.org/10.1175/JPO-D-14-0157.1>.
- , R. J. Small, F. O. Bryan, and R. A. Tomas, 2017: Scale dependence of mid-latitude air–sea interaction. *J. Climate*, **30**, 8207–8221, <https://doi.org/10.1175/JCLI-D-17-0159.1>.
- Cane, M. A., A. C. Clement, L. Murphy, and K. Bellomo, 2017: Low-pass filtering, heat flux, and Atlantic multidecadal variability. *J. Climate*, **30**, 7529–7553, <https://doi.org/10.1175/JCLI-D-16-0810.1>.
- Cayan, D. R., 1992: Variability of latent and sensible heat fluxes estimated using bulk formulae. *Atmos.–Ocean*, **30**, 1–42, <https://doi.org/10.1080/07055900.1992.9649429>.
- Chelton, D. B., R. A. deSzoeke, M. G. Schlax, K. E. Naggar, and N. Siwertz, 1998: Geographical variability of the first baroclinic Rossby radius of deformation. *J. Phys. Oceanogr.*, **28**, 433–460, [https://doi.org/10.1175/1520-0485\(1998\)028<0433:GVOTFB>2.0.CO;2](https://doi.org/10.1175/1520-0485(1998)028<0433:GVOTFB>2.0.CO;2).
- , and Coauthors, 2001: Observations of coupling between surface wind stress and sea surface temperature in the eastern tropical Pacific. *J. Climate*, **14**, 1479–1498, [https://doi.org/10.1175/1520-0442\(2001\)014<1479:OOCBSW>2.0.CO;2](https://doi.org/10.1175/1520-0442(2001)014<1479:OOCBSW>2.0.CO;2).
- , M. G. Schlax, and R. M. Samelson, 2011: Global observations of nonlinear mesoscale eddies. *Prog. Oceanogr.*, **91**, 167–216, <https://doi.org/10.1016/j.pocan.2011.01.002>.
- Chin, T. M., J. Vazquez-Cuervo, and E. M. Armstrong, 2017: A multi-scale high-resolution analysis of global sea surface temperature. *Remote Sens. Environ.*, **200**, 154–169, <https://doi.org/10.1016/j.rse.2017.07.029>.
- Clayson, C. A., and A. S. Bogdanoff, 2013: The effect of diurnal sea surface temperature warming on climatological air–sea fluxes. *J. Climate*, **26**, 2546–2556, <https://doi.org/10.1175/JCLI-D-12-00062.1>.
- Clement, A., K. Bellomo, L. N. Murphy, M. A. Cane, T. Mauritsen, G. Rädel, and B. Stevens, 2015: The Atlantic multidecadal oscillation without a role for ocean circulation. *Science*, **350**, 320–324, <https://doi.org/10.1126/science.aab3980>.
- Cohen, J., and P. Cohen, 1983: *Applied Multiple Regression/Correlation Analysis for the Behavioral Sciences*. Lawrence Erlbaum Associates, 545 pp.
- Delworth, T. L., and Coauthors, 2012: Simulated climate change in the GFDL CM2.5 high-resolution coupled climate model. *J. Climate*, **25**, 2755–2781, <https://doi.org/10.1175/JCLI-D-11-00316.1>.
- , F. Zeng, L. Zhang, R. Zhang, G. A. Vecchi, and X. Yang, 2017: The central role of ocean dynamics in connecting the North Atlantic Oscillation to the extratropical component of the Atlantic multidecadal oscillation. *J. Climate*, **30**, 3789–3805, <https://doi.org/10.1175/JCLI-D-16-0358.1>.
- Doney, S. C., S. Yeager, G. Danabasoglu, W. G. Large, and J. C. McWilliams, 2007: Mechanisms governing interannual variability of upper-ocean temperature in a global ocean hindcast simulation. *J. Phys. Oceanogr.*, **37**, 1918–1938, <https://doi.org/10.1175/JPO3089.1>.
- Donlon, C., and Coauthors, 2007: The global ocean data assimilation experiment high-resolution sea surface temperature pilot project. *Bull. Amer. Meteor. Soc.*, **88**, 1197–1213, <https://doi.org/10.1175/BAMS-88-8-1197>.
- Fairall, C. W., E. F. Bradley, D. P. Rogers, J. B. Edson, and G. S. Young, 1996: Bulk parameterization of air–sea fluxes for Tropical Ocean–Global Atmosphere Coupled Ocean–Atmosphere Response Experiment. *J. Geophys. Res.*, **101**, 3747–3764, <https://doi.org/10.1029/95JC03205>.
- , —, J. E. Hare, A. A. Grachev, and J. B. Edson, 2003: Bulk parameterization of air–sea fluxes: Updates and verification for the COARE algorithm. *J. Climate*, **16**, 571–591, [https://doi.org/10.1175/1520-0442\(2003\)016<0571:BPOASF>2.0.CO;2](https://doi.org/10.1175/1520-0442(2003)016<0571:BPOASF>2.0.CO;2).
- Frankignoul, C., and K. Hasselmann, 1977: Stochastic climate models. II: Application of sea surface temperature anomalies and thermocline variability. *Tellus*, **29**, 289–305, <https://doi.org/10.3402/tellusa.v29i4.11362>.
- , and E. Kestenare, 2002: The surface heat flux feedback. Part 1: Estimate from observations in the Atlantic and the North Pacific. *Climate Dyn.*, **19**, 633–647, <https://doi.org/10.1007/s00382-002-0252-x>.
- , N. Sennechal, Y.-O. Kwon, and M. A. Alexander, 2011: Influence of the meridional shifts of the Kuroshio and the Oyashio Extensions on the atmospheric circulation. *J. Climate*, **24**, 762–777, <https://doi.org/10.1175/2010JCLI3731.1>.
- Gent, P. R., and J. C. McWilliams, 1990: Isopycnal mixing in ocean circulation models. *J. Phys. Oceanogr.*, **20**, 150–155, [https://doi.org/10.1175/1520-0485\(1990\)020<0150:MIIOC>2.0.CO;2](https://doi.org/10.1175/1520-0485(1990)020<0150:MIIOC>2.0.CO;2).
- Griffies, S., and Coauthors, 2015: Impacts on ocean heat from transient mesoscale eddies in a hierarchy of climate models. *J. Climate*, **28**, 952–977, <https://doi.org/10.1175/JCLI-D-14-00353.1>.
- Gulev, S. K., M. Latif, N. Keenlyside, W. Park, and K.-P. Koltermann, 2013: North Atlantic Ocean control on surface heat flux on multidecadal timescales. *Nature*, **499**, 464–467, <https://doi.org/10.1038/nature12268>.

- Hausmann, U., A. Czaja, and J. Marshall, 2017: Mechanisms controlling the SST air–sea heat flux feedback and its dependence on spatial scale. *Climate Dyn.*, **48**, 1297–1307, <https://doi.org/10.1007/s00382-016-3142-3>.
- Hunke, E. C., and W. H. Lipscomb, 2008: CICE: The Los Alamos sea ice model user's manual, version 4. Los Alamos National Laboratory Tech. Rep. LA-CC-06-012, 76 pp.
- Hurrell, J. W., and Coauthors, 2013: The Community Earth System Model: A framework for collaborative research. *Bull. Amer. Meteor. Soc.*, **94**, 1339–1360, <https://doi.org/10.1175/BAMS-D-12-00121.1>.
- Jin, X., and L. Yu, 2013: Assessing high-resolution analysis of surface heat fluxes in the Gulf Stream region. *J. Geophys. Res. Oceans*, **118**, 5353–5375, <https://doi.org/10.1002/jgrc.20386>.
- Kalnay, E., and Coauthors, 1996: The NCEP/NCAR 40-Year Reanalysis Project. *Bull. Amer. Meteor. Soc.*, **77**, 437–471, [https://doi.org/10.1175/1520-0477\(1996\)077<0437:TNYRP>2.0.CO;2](https://doi.org/10.1175/1520-0477(1996)077<0437:TNYRP>2.0.CO;2).
- Kanamitsu, M., W. Ebisuzaki, J. Woollen, S.-K. Yang, J. J. Hnilo, M. Fiorino, and G. L. Potter, 2002: NCEP–DOE AMIP II Reanalysis (R-2). *Bull. Amer. Meteor. Soc.*, **83**, 1631–1643, <https://doi.org/10.1175/BAMS-83-11-1631>.
- Kirtman, B. P., and Coauthors, 2012: Impact of ocean model resolution on CCSM climate simulations. *Climate Dyn.*, **39**, 1303–1328, <https://doi.org/10.1007/s00382-012-1500-3>.
- Kubota, M., N. Iwasaka, S. Kizu, M. Kondo, and K. Kutsuwada, 2002: Japanese ocean flux datasets with use of remote sensing observations (J-OFURO). *J. Oceanogr.*, **58**, 213–225, <https://doi.org/10.1023/A:1015845321836>.
- Kuo, Y.-H., R. J. Reed, and S. Low-Nam, 1991: Effects of surface energy fluxes during the early development and rapid intensification stages of seven explosive cyclones in the western Atlantic. *Mon. Wea. Rev.*, **119**, 457–475, [https://doi.org/10.1175/1520-0493\(1991\)119<0457:EOSEFD>2.0.CO;2](https://doi.org/10.1175/1520-0493(1991)119<0457:EOSEFD>2.0.CO;2).
- Large, W. G., and S. G. Yeager, 2004: Diurnal to decadal global forcing for ocean and sea-ice models: The data sets and flux climatologies. NCAR Tech. Note NCAR/TN-460+STR, 105 pp., <http://opensky.ucar.edu/islandora/object/technotes:434>.
- , and —, 2009: The global climatology of an interannually varying air–sea flux data set. *Climate Dyn.*, **33**, 341–364, <https://doi.org/10.1007/s00382-008-0441-3>.
- Laurindo, L. C., L. Siqueira, A. J. Mariano, and B. P. Kirtman, 2018: Cross-spectral analysis of the SST/10 m wind speed coupling resolved by satellite products and climate model simulations. *Climate Dyn.*, <https://doi.org/10.1007/s00382-018-4434-6>.
- Lawrence, D. M., and Coauthors, 2011: Parameterization improvements and functional and structural advances in Version 4 of the Community Land Model. *J. Adv. Model. Earth Syst.*, **3**, M03001, <https://doi.org/10.1029/2011MS00045>.
- Liu, W. T., K. B. Katsaros, and J. A. Businger, 1979: Bulk parameterization of air–sea exchanges of heat and water vapor including the molecular constraints at the interface. *J. Atmos. Sci.*, **36**, 1722–1735, [https://doi.org/10.1175/1520-0469\(1979\)036<1722:BPOASE>2.0.CO;2](https://doi.org/10.1175/1520-0469(1979)036<1722:BPOASE>2.0.CO;2).
- Ma, X., and Coauthors, 2016: Western boundary currents regulated by interaction between ocean eddies and the atmosphere. *Nature*, **535**, 533–537, <https://doi.org/10.1038/nature18640>.
- , P. Chang, R. Saravanan, R. Montuoro, H. Nakamura, D. Wu, X. Lin, and L. Wu, 2017: Importance of resolving Kuroshio front and eddy influence in simulating the North Pacific storm track. *J. Climate*, **30**, 1861–1880, <https://doi.org/10.1175/JCLI-D-16-0154.1>.
- Madden, R. A., and P. R. Julian, 1994: Observations of the 40–50-day tropical oscillation—A review. *Mon. Wea. Rev.*, **122**, 814–837, [https://doi.org/10.1175/1520-0493\(1994\)122<0814:OOTDTC>2.0.CO;2](https://doi.org/10.1175/1520-0493(1994)122<0814:OOTDTC>2.0.CO;2).
- Marshall, J., and Coauthors, 2009: The CLIMODE field campaign: Observing the cycle of convection and restratification over the Gulf Stream. *Bull. Amer. Meteor. Soc.*, **90**, 1337–1350, <https://doi.org/10.1175/2009BAMS2706.1>.
- Martin, M., and Coauthors, 2012: Group for High Resolution Sea Surface Temperature (GHRSSST) analysis fields inter-comparisons. Part 1: A GHRSSST multi-product ensemble (GMPE). *Deep-Sea Res. II*, **77–80**, 21–30, <https://doi.org/10.1016/j.dsr2.2012.04.013>.
- O'Reilly, C. H., and L. Zanna, 2018: The signature of oceanic processes in decadal extratropical SST anomalies. *Geophys. Res. Lett.*, **45**, 7719–7730, <https://doi.org/10.1029/2018GL079077>.
- Park, S., C. Deser, and M. A. Alexander, 2005: Estimation of the surface heat flux response to sea surface temperature anomalies over the global oceans. *J. Climate*, **18**, 4582–4599, <https://doi.org/10.1175/JCLI3521.1>.
- , C. S. Bretherton, and P. J. Rasch, 2014: Integrating cloud processes in the Community Atmosphere Model, version 5. *J. Climate*, **27**, 6821–6856, <https://doi.org/10.1175/JCLI-D-14-00087.1>.
- Putrasahan, D. A., I. Kamenkovich, M. LeHénaff, and B. P. Kirtman, 2017: Importance of ocean mesoscale variability for air–sea interactions in the Gulf of Mexico. *Geophys. Res. Lett.*, **44**, 6352–6362, <https://doi.org/10.1002/2017GL072884>.
- Reynolds, R. W., and D. B. Chelton, 2010: Comparisons of daily sea surface temperature analyses for 2007–08. *J. Climate*, **23**, 3545–3562, <https://doi.org/10.1175/2010JCLI3294.1>.
- , T. M. Smith, C. Liu, D. B. Chelton, K. S. Casey, and M. G. Schlax, 2007: Daily high-resolution-blended analyses for sea surface temperature. *J. Climate*, **20**, 5473–5496, <https://doi.org/10.1175/2007JCLI1824.1>.
- , D. B. Chelton, J. Roberts-Jones, M. J. Martin, D. Menemenlis, and C. J. Merchant, 2013: Objective determination of feature resolution in two sea surface temperature analyses. *J. Climate*, **26**, 2514–2533, <https://doi.org/10.1175/JCLI-D-12-00787.1>.
- Roberts, J. B., C. A. Clayson, F. R. Robertson, and D. L. Jackson, 2010: Predicting near-surface atmospheric variables from Special Sensor Microwave/Imager using neural networks with a first-guess approach. *J. Geophys. Res.*, **115**, D19113, <https://doi.org/10.1029/2009JD013099>.
- Roberts, M. J., H. T. Hewitt, P. Hyder, D. Ferreira, S. A. Josey, M. Mizielinski, and A. Shelly, 2016: Impact of ocean resolution on coupled air–sea fluxes and large-scale climate. *Geophys. Res. Lett.*, **43**, 10 430–10 438, <https://doi.org/10.1002/2016GL070559>.
- Saji, N. H., and T. Yamagata, 2003: Structure of SST and surface wind variability during Indian Ocean dipole mode events: COADS observations. *J. Climate*, **16**, 2735–2751, [https://doi.org/10.1175/1520-0442\(2003\)016<2735:SOSASW>2.0.CO;2](https://doi.org/10.1175/1520-0442(2003)016<2735:SOSASW>2.0.CO;2).
- Schneider, N., and B. Qiu, 2015: The atmospheric response to weak sea surface temperature fronts. *J. Atmos. Sci.*, **72**, 3356–3377, <https://doi.org/10.1175/JAS-D-14-0212.1>.
- Sérazin, G., T. Penduff, S. Grégorio, B. Barnier, J.-M. Molines, and L. Terray, 2015: Intrinsic variability of sea level from global 1/2 simulations: Spatiotemporal scales. *J. Climate*, **28**, 4279–4292, <https://doi.org/10.1175/JCLI-D-14-00554.1>.
- Small, R. J., and Coauthors, 2008: Air–sea interaction over ocean fronts and eddies. *Dyn. Atmos. Oceans*, **45**, 274–319, <https://doi.org/10.1016/j.dynatmoce.2008.01.001>.
- , and Coauthors, 2014: A new synoptic scale resolving global climate simulation using the Community Earth System Model. *J. Adv. Model. Earth Syst.*, **6**, 1065–1094, <https://doi.org/10.1002/2014MS000363>.



- Smirnov, D., M. Newman, and M. A. Alexander, 2014: Investigating the role of ocean–atmosphere coupling in the North Pacific Ocean. *J. Climate*, **27**, 592–606, <https://doi.org/10.1175/JCLI-D-13-00123.1>.
- , —, —, Y. Kwon, and C. Frankignoul, 2015: Investigating the local atmospheric response to a realistic shift in the Oya-shio sea surface temperature front. *J. Climate*, **28**, 1126–1147, <https://doi.org/10.1175/JCLI-D-14-00285.1>.
- Smith, R. D., and Coauthors, 2010: The Parallel Ocean Program (POP) reference manual. Los Alamos National Laboratory Tech. Rep. LAUR-10-01853, 140 pp.
- Tanimoto, Y., H. Nakamura, T. Kagimoto, and S. Yamane, 2003: An active role of extratropical sea surface temperature anomalies in determining anomalous turbulent heat flux. *J. Geophys. Res.*, **108**, 3304, <https://doi.org/10.1029/2002JC001750>.
- Tomita, H., M. Kubota, M. F. Cronin, S. Iwasaki, M. Konda, and H. Ichikawa, 2010: An assessment of surface heat fluxes from J-OFURO2 at the KEO and JKEO sites. *J. Geophys. Res.*, **115**, C03018, <https://doi.org/10.1029/2009JC005545>.
- , T. Hihara, S. Kato, M. Kubota, and K. Kutsuwada, 2019: An introduction to J-OFURO3, a third-generation Japanese ocean flux data set using remote-sensing observations. *J. Oceanogr.*, **75**, 171–194, <https://doi.org/10.1007/s10872-018-0493-x>.
- Uppala, S. M., and Coauthors, 2005: The ERA-40 Re-Analysis. *Quart. J. Roy. Meteor. Soc.*, **131**, 2961–3012, <https://doi.org/10.1256/qj.04.176>.
- von Storch, J.-S., 2000: Signatures of air–sea interactions in a coupled atmosphere–ocean GCM. *J. Climate*, **13**, 3361–3379, [https://doi.org/10.1175/1520-0442\(2000\)013<3361:SOASII>2.0.CO;2](https://doi.org/10.1175/1520-0442(2000)013<3361:SOASII>2.0.CO;2).
- Wu, R., B. P. Kirtman, and K. Pegion, 2006: Local air–sea relationship in observations and model simulations. *J. Climate*, **19**, 4914–4932, <https://doi.org/10.1175/JCLI3904.1>.
- Xie, S.-P., 2004: Satellite observations of cool ocean–atmosphere interaction. *Bull. Amer. Meteor. Soc.*, **85**, 195–208, <https://doi.org/10.1175/BAMS-85-2-195>.
- , M. Ishiwatari, H. Hashizume, and K. Takeuchi, 1998: Coupled ocean–atmospheric waves on the equatorial front. *Geophys. Res. Lett.*, **25**, 3863–3866, <https://doi.org/10.1029/1998GL900014>.
- Yu, L., and R. A. Weller, 2007: Objectively analyzed air–sea heat fluxes for the global ice-free oceans (1981–2005). *Bull. Amer. Meteor. Soc.*, **88**, 527–539, <https://doi.org/10.1175/BAMS-88-4-527>.
- Zhang, R., R. Sutton, G. Danabasoglu, T. L. Delworth, W. M. Kim, J. Robson, and S. G. Yeager, 2016: Comment on “The Atlantic multidecadal oscillation without a role for ocean circulation.” *Science*, **352**, 1527, <https://doi.org/10.1126/science.aaf1660>.
- , X. Wang, and C. Wang, 2018: On the simulations of global oceanic latent heat flux in the CMIP5 multimodel ensemble. *J. Climate*, **31**, 7111–7128, <https://doi.org/10.1175/JCLI-D-17-0713.1>.